



BRNO UNIVERSITY OF TECHNOLOGY
VYSOKÉ UČENÍ TECHNICKÉ V BRNĚ

FACULTY OF INFORMATION TECHNOLOGY
FAKULTA INFORMAČNÍCH TECHNOLOGIÍ

DEPARTMENT OF COMPUTER GRAPHICS AND MULTIMEDIA
ÚSTAV POČÍTAČOVÉ GRAFIKY A MULTIMÉDIÍ

**MEASURING THE THICKNESS OF CONTAMINATION
LAYERS IN SCANNING ELECTRON MICROSCOPY
USING IMAGE PROCESSING**
MĚŘENÍ TLOUŠŤKY KONTAMINAČNÍCH VRSTEV VE SKENOVACÍ ELEKTRONOVÉ MIKROSKOPII
POMOCÍ ZPRACOVÁNÍ OBRAZU

BACHELOR'S THESIS
BAKALÁŘSKÁ PRÁCE

AUTHOR
AUTOR PRÁCE

MATĚJ MACEK

SUPERVISOR
VEDOUCÍ PRÁCE

doc. Ing. MARTIN ČADÍK, Ph.D.

BRNO 2024

Bachelor's Thesis Assignment



Institut: Department of Computer Graphics and Multimedia (DCGM) 156288
Student: **Macek Matěj**
Programme: Information Technology
Title: **Measuring the thickness of contamination layers in scanning electron microscopy using image processing**
Category: Computer vision
Academic year: 2023/24

Assignment:

1. Acquire basic understanding of scanning electron microscopy (SEM) and the characteristics of secondary electron (SE) images.
2. Explore state of the art techniques for measuring features in the image (in context of measuring thickness of deposited material).
3. Propose or improve techniques for measuring the thickness of contamination layers formed on the specimen by extended electron exposure using image processing.
4. Put the proposed methods into practice and execute the measurements on SEM SE images.
5. Evaluate proposed methods and discuss the obtained results.
6. Present your results in the form of a poster and a short video.

Literature:

- Ritchie, Nicholas W. M., et al. Scanning Electron Microscopy and X-Ray Microanalysis. 4th ed., Springer, 2017.
- Gonzalez, R. C. and Woods, R. E., Digital image processing, Prentice Hall , Upper Saddle River, N.J., 2008.

Requirements for the semestral defence:

Points 1-3 of the assignment.

Detailed formal requirements can be found at <https://www.fit.vut.cz/study/theses/>

Supervisor: **Čadík Martin, doc. Ing., Ph.D.**
Head of Department: Černocký Jan, prof. Dr. Ing.
Beginning of work: 1.11.2023
Submission deadline: 9.5.2024
Approval date: 9.11.2023

Abstract

The motivation for this thesis arises from the aim of the Thermo Fisher Scientific company to develop a method to measure the thickness of contamination layers in scanning electron microscopy (SEM) images through advanced image processing techniques. The primary aim is to create automated methods for quantifying contamination in images that adversely impact imaging in material science research, using image processing techniques. In this study, we collect a dataset of images with contamination and manually annotate masks for each image. These annotations will serve to fine-tune and evaluate the effectiveness of the methods we propose. By employing a combination of edge detection algorithms and machine learning models, specifically a fine-tuned DeepLabv3 network, this work enhances the precision and efficiency for contamination detection. The edge Detection-Based Contamination Analyzer (EDCA) utilizes traditional image processing methods, while the DeepLabv3 model introduces a machine learning approach to robustly handle diverse imaging conditions. Comparative analyses demonstrate the effectiveness of these methods in providing reliable, scalable, and detailed measurements of contamination layers, significantly contributing to the field of materials science.

Abstrakt

Motivací pro vznik této práce byl cíl společnosti Thermo Fisher Scientific vyvinout metodu měření tloušťky kontaminačních vrstev na snímcích ze skenovací elektronové mikroskopie (SEM) pomocí pokročilých technik zpracování obrazu. Hlavním cílem je vytvořit automatizované metody pro kvantifikaci kontaminace v obrazech, které nepříznivě ovlivňují zobrazení ve výzkumu v oblasti materiálových věd, pomocí technik zpracování obrazu. V této studii shromažďujeme soubor dat snímků s kontaminací a ručně anotujeme masky pro každý snímek. Tyto anotace budou sloužit k doladění a využití účinnosti námi navrhovaných metod. Použitím kombinace algoritmů detekce hran a modelů strojového učení, konkrétně vyladěné sítě DeepLabv3, tato práce zvyšuje přesnost a účinnost detekce kontaminace. Analyzátor kontaminace založený na detekci hran (EDCA) využívá tradiční metody zpracování obrazu, zatímco model DeepLabv3 zavádí přístup strojového učení, který robustně zvládá různorodé obrazové podmínky. Srovnávací analýzy prokazují účinnost těchto metod při poskytování spolehlivých, škálovatelných a podrobných měření kontaminačních vrstev, což významně přispívá k rozvoji oboru materiálových věd.

Keywords

Scanning Electron Microscopy (SEM), Image Processing, Contamination Thickness Measurement, Edge Detection, Machine Learning, DeepLabv3, Material Science

Klíčová slova

Rastrovací elektronová mikroskopie (SEM), zpracování obrazu, měření tloušťky kontaminace, detekce hran, strojové učení, DeepLabv3, studie materiálů

Reference

MACEK, Matěj. *Measuring the thickness of contamination layers in scanning electron microscopy using image processing*. Brno, 2024. Bachelor's thesis. Brno University of Technology, Faculty of Information Technology. Supervisor doc. Ing. Martin Čadík, Ph.D.

Rozšířený abstrakt

Motivace pro tuto práci vychází ze závazku společnosti Thermo Fisher Scientific k rozvoji technologií používaných v rastrovací elektronové mikroskopii (SEM). Společnost si klade za cíl vyvinout automatizovanou metodu pro měření tloušťky kontaminačních vrstev na vzorcích analyzovaných pomocí SEM, která by měla být praktičtější ve srovnání se stávajícími manuálními metodami. V současnosti neexistuje automatická metoda, která by tuto úlohu mohla vykonávat, což představuje významné omezení v oblasti materiálové vědy. Přesné a efektivní měření kontaminace je klíčové, protože ovlivňuje kvalitu obrazů SEM a tím i spolehlivost charakterizace a analýzy materiálů. Tento výzkum se snaží řešit tyto výzvy vývojem nové automatizované měřicí techniky.

Definice problému: Hlavní výzvou tohoto výzkumu je vývoj spolehlivé automatizované metody pro měření tloušťky kontaminačních vrstev pomocí technik zpracování obrazu. Současné metody často vyžadují manuální zásah, což může být časově náročné a náchylné k lidské chybě. Navíc je složitost úkolu zvýšena nekonzistencí v obrazech kontaminace; SEM obrazy různých vzorků mohou vykazovat široké spektrum rysů kontaminace, jako jsou různé tloušťky, hustoty a dokonce i vizuální aspekty v závislosti na látce a environmentálních podmínkách během přípravy a zkoumání vzorku. Tato diverzita vyžaduje robustní algoritmy, které jsou schopné přesně měřit kontaminaci napříč různorodými obrazy bez ztráty přesnosti.

Existující řešení: Pokrok v metodách kvantifikace kontaminace indukované elektronovým paprskem v elektronových mikroskopech přinesl užitečné přístupy k hodnocení a minimalizaci kontaminace. Roediger et al. [22] vyvinuli automatizovanou metodu zaměřující se na měření kontaminace v komoře skenovacích elektronových mikroskopů, která využívá depozici materiálu z plynu na substrát pod kontrolou podmínek a atomického mikroskopu. Tento přístup umožňuje kontinuální sledování úrovní kontaminace a poskytuje data pro optimalizaci čistoty komory a údržbových plánů. Hugenschmidt et al. [9] poukázali na schopnosti technologií specifických pro STEM, jako je High Angular Annular Dark Field (HAADF), měřit kontaminaci prostřednictvím vizualizace vysoce kontrastních obrazů přímo spojených s atomovým číslem prvků. Tyto pokročilé techniky však vyžadují speciální komponenty v mikroskopu, které nejsou vždy součástí a podmínky pro měření jsou odlišné od našich, kde my využíváme vzorek s cínovými kuličkami, kde následně skenujeme delší dobu na stejném místě a časem vznikne nahromaděná vrstva kontaminace, která má jasně viditelnou boční hranu kvůli sférickému tvaru cínové kuličky.

Navržené řešení a implementace metod: Tato práce představuje Analyzátor kontaminace založený na detekci hran (EDCA), speciálně navržený pro SEM obrazy, zahrnující pokročilé techniky předzpracování obrazu a využívání operátoru Scharr k určení oblastí zájmu (ROI). Proces zahrnuje snižování šumu pomocí Gaussova rozostření, morfologické operace pro zlepšení kvality obrazu a detekci hran pro přesnou identifikaci hranic vrstev kontaminace. Analýzou gradientu a vertikálním profilováním přesně identifikujeme horní a dolní hranice vrstev kontaminace z centrálního sloupce kontaminace, což nastavuje výchozí bod pro detekci hranic na základě první derivace vertikálního profilu linie. Kromě toho implementujeme model založený na architektuře DeepLabv3, původně předtrénovaný na rozmanitých datech, který je doladěn pro zlepšení schopností segmentace speciálně pro SEM obrazy kontaminace. Tento přístup efektivně rozlišuje mezi kontaminovanými a nekontaminovanými oblastmi. Model je dále optimalizován úpravou jeho rychlosti učení a ztrátové funkce, aby odpovídá našemu konkrétnímu úkolu binární klasifikace, čímž zajišťuje robustní učení a konzistentní výkon napříč novými a dosud neviděnými SEM obrazy. Detailní implementace těchto metod zahrnuje přípravu datasetu a anotaci, konfiguraci modelu a

postprocesing, který umožňuje efektivní naučení modelu a jeho schopnost generalizace na nové, neviděné obrázky.

Experimenty a výsledky: Provedli jsme experimenty s různými datasety za účelem hodnocení vlivu ladění na výkon modelu při měření tloušťky kontaminační vrstvy v SEM snímcích. Byly hodnoceny dvě metodiky: Analyzátor kontaminace založený na detekci hran (EDCA) a laděný model DeepLabv3, přičemž byla zaměřena pozornost na jejich přesnost, preciznost a metriky chyb ve srovnání s ručně anotovanými daty. Experimenty zahrnovaly datasety s kontaminací, smíšené datasety a augmentované datasety. Bylo zjištěno, že malý počet epoch při tréninku je efektivní a zabraňuje nadměrnému přizpůsobení modelu. Optimalizace prahových hodnot pro získání kontaminace z pravděpodobnostní masky byla klíčová pro kalibraci modelů, aby přesně segmentovaly kontaminované oblasti. Model laděný na augmentovaném datasetu dosáhl průměrné hodnoty IoU 0.832 se směrodatnou odchylkou 0.071 a byl ohodnocen jako nejlepší ze všech se kterými jsme experimentovali. Průměrná chyba v nanometrech byla vypočítána pro výsledek výšky každé metody na unikátním datasetu, kde EDCA zaznamenala 7.9 nm a model DeepLabv3 7.27 nm, což ukazuje na lepší výkonnost modelu. V porovnání dosáhl model úspěšnosti 98.16% na unikátním datasetu, zatímco EDCA dosáhla 87.16%, což demonstruje významnou robustnost modelu.

Závěr: Tato studie hodnotí účinnost dvou metod pro měření tloušťky kontaminačních vrstev ve skenovací elektronové mikroskopii: tradiční metodu založenou na detekci hran a metodu s využitím strojového učení a modelu založeném na architektuře DeepLabv3. Model, laděný na augmentovaném datasetu, ukázal vyšší přesnost a efektivitu ve srovnání s tradičním přístupem. Výsledky naznačují, že tento model nabízí významné výhody pro přesnou analýzu SEM obrázků a poskytuje vhodný nástroj pro použití v praxi.

Measuring the thickness of contamination layers in scanning electron microscopy using image processing

Declaration

I hereby declare that this Bachelor's thesis was prepared as an original work by the author under the supervision of doc. Ing. Martina Čadíka Ph.D.. The supplementary information was provided by Dr. Manuel Bornhoeft. I have listed all the literary sources, publications and other sources, which were used during the preparation of this thesis.

.....
Matěj Macek
May 7, 2024

Acknowledgements

I would like to express my gratitude to my supervisor doc. Ing. Martin Čadík, Ph.D., for his invaluable guidance and support throughout this research. I also extend my thanks to Dr. Manuel Bornhoeft for his insightful consultations, which have significantly contributed to the development of this work. Their expertise and assistance were crucial in shaping the methodologies and execution of this work. I am also grateful to Thermo Fisher Scientific Brno s.r.o. for their support and the resources they provided, which were instrumental in the success of this research. In the last part, I would like to express my gratitude for the language assistance provided by ChatGPT[17], an AI developed by OpenAI, which helped in paraphrasing portions of the text to enhance the clarity and coherence of this thesis.

Contents

| | | |
|----------|--------------------------------------------------------------------------|-----------|
| 1 | Introduction | 2 |
| 2 | Scanning Electron Microscopy | |
| | Secondary Electron Image Characteristics | 3 |
| 2.1 | Introduction to Scanning Electron Microscopy (SEM) | 3 |
| 2.2 | Formation of Secondary Electron (SE) Images | 4 |
| 2.3 | Characteristics of SE Images | 5 |
| 2.4 | Contamination in SEM | 6 |
| 3 | Measuring Features in SEM Images | 10 |
| 3.1 | Measuring Chamber Contamination in SEM | 10 |
| 3.2 | Image Analysis for Contamination Assessment | 11 |
| 3.3 | Conclusion | 15 |
| 4 | Proposed Methods for Measuring Contamination Layer Thickness | 16 |
| 4.1 | Evaluation of Existing Methods and The Need for New Approaches | 16 |
| 4.2 | Proposed Methods | 17 |
| 4.2.1 | Edge Detection-Based Contamination Analyzer (EDCA) | 17 |
| 4.2.2 | DeepLabv3-based Contamination Layer Segmentation | 17 |
| 5 | Data Collection and Analysis | 18 |
| 5.1 | Data Collection | 18 |
| 5.2 | Annotation Dataset and Automatic Tests | 20 |
| 5.3 | Automated Testing of Image Analysis Algorithms | 21 |
| 5.4 | Data Augmentation | 22 |
| 5.5 | Automation Mask Threshold Finder | 25 |
| 6 | Implementation of Proposed Methods | 28 |
| 6.1 | Method 1: Edge Detection-Based Contamination Analyzer (EDCA) | 28 |
| 6.2 | Method 2: DeepLabv3-based Contamination Layer Segmentation | 32 |
| 7 | Experiments and Evaluation | 36 |
| 7.1 | Model Experiments Across Datasets | 36 |
| 7.2 | Error Analysis | 40 |
| 7.3 | The precision of each method | 44 |
| 8 | Conclusion and Future Work | 46 |
| | Bibliography | 48 |

Chapter 1

Introduction

Contamination in Scanning Electron Microscopy (SEM) poses significant challenges in the microscopic analysis of materials. Such contamination, often manifested as unwanted deposits on the specimen surface, can significantly obscure microscopic features and interfere with the electron beam, thus degrading the quality of the SEM images. Understanding and mitigating the effects of contamination is crucial for ensuring the reliability and accuracy of SEM-based investigations.

This thesis focuses on the critical issue of contamination in SEM. It explores various methods for detecting and quantifying contamination, which is vital for improving the image quality and the interpretative accuracy of SEM analyses. The primary objective is to develop and assess different computational techniques that can automate the detection and measurement of contamination layers with high precision and minimal human intervention.

To achieve this, the thesis proposes two novel approaches: an advanced image processing algorithm Edge Detection-Based Contamination Analyzer (EDCA), and a machine learning model adapted from the DeepLabv3 architecture. Both methods are designed to enhance detection capabilities by accurately segmenting and quantifying contamination from SEM images without any operator.

It is crucial to create and meticulously annotate the datasets to measure contamination and test the effectiveness of the proposed methods. This annotation process involves labeling the areas of contamination in the SEM images to train and validate the computational models effectively. These annotated datasets will encompass SEM images with varying degrees of contamination to provide a robust foundation for the experimental evaluation. The experiments will not only compare the proposed methods against traditional manual measurements but also explore the impact of different training regimes and data augmentation techniques on the performance of the machine learning model.

Ultimately, this study aims to provide a detailed comparative analysis of the proposed methods, offering insights into their practical applications and limitations in the context of SEM. The findings are expected to contribute significantly to the field of electron microscopy by providing robust tools for contamination analysis, thereby enhancing build a foundation to enhance the overall quality and efficacy of SEM imaging in future contamination mitigation.

Chapter 2

Scanning Electron Microscopy Secondary Electron Image Characteristics

In this chapter, we describe the fundamental principles of Scanning Electron Microscopy (SEM) and explore the generation and characteristics of secondary electrons, as well as aspects of SEM imaging. This chapter provides an overview of the functions of an SEM within the context of this thesis. For a more detailed exploration of SEM technologies and applications, readers are encouraged to consult *Scanning Electron Microscopy and X-ray Microanalysis* [7].

2.1 Introduction to Scanning Electron Microscopy (SEM)

The scanning electron microscope (SEM) is a sophisticated device designed to create magnified images that elucidate microscopic details such as the size, shape, composition and other physical and chemical properties of the specimens. The SEM operates by generating a finely focused beam of electrons, typically with energies ranging from 0.1 to 30 keV, which is emitted from an electron source. The high energies of the electrons are related to their small wavelengths, which enable nanometer-resolution imaging. This beam is precisely shaped and directed by apertures, magnetic and electrostatic lenses, and electromagnetic coils, enabling it to scan the specimen in a controlled raster (x - y) pattern see fig 2.1.

The interaction of the electron beam with the specimen at various discrete points results in the emission of two primary types of electrons: backscattered electrons (BSEs), which are electrons that maintain most of their initial energy after deflecting off the specimen's atoms, and secondary electrons (SEs), which are ejected from the specimen's atoms with considerably lower energies, typically below 5 eV. These electrons are detected by specialized detectors, including the Everhart–Thornley detector for secondary electrons and dedicated detectors for backscattered electrons. The signals from these detectors are digitized and used to form the image pixels, reflecting the intensity of the detected signals at each scan point. In further of the thesis, we will only focus on secondary electrons which are important for our work. Further, this thesis concentrates on the study and application of Secondary Electrons (SE) for their significant role in the analytical techniques we have implemented.

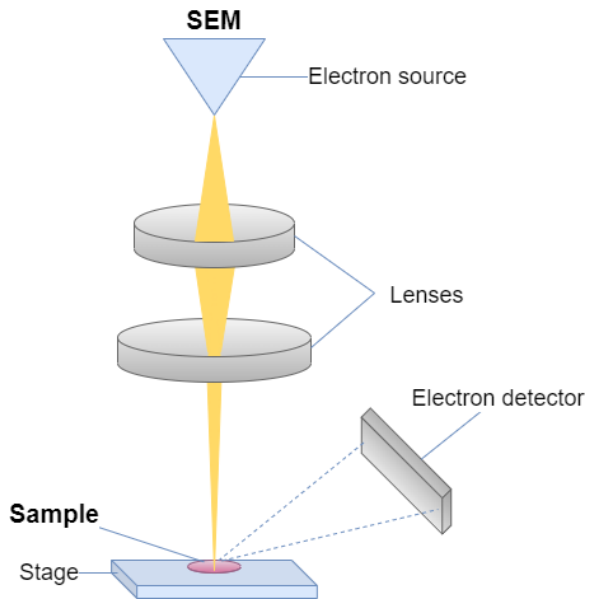


Figure 2.1: An illustration displaying schematic diagram of scanning electron microscopes. In SEM, the electron beam raster-scans across the sample surface, and detectors collect the electrons emitted from the surface.

Operating Principles of SEM

Scanning electron microscopes (SEMs) use an electron beam to obtain high-definition images of specimens up to the nanometer scale. The electrons are produced from a filament and meticulously arranged into a focused beam in the electron source. Following this, a sequence of lenses in the electron column is used to focus and steer this beam onto the specimen's surface.

Beam Quality and Vacuum Environment

The operation of SEM (Scanning Electron Microscope) often necessitates a high vacuum environment, typically below 10^{-4} Pa, to maintain the integrity of the focused primary electron beam. This vacuum minimizes the scattering of the electron beam by atmospheric gases and avoids the collisions between the beam electrons and residual gas molecules. Such interactions can cause elastic-scattering events, degrading the image quality and resolution due to reduced beam intensity and uneven scattering along the beam path. Conversely, variable pressure SEMs (VPSEM) facilitate the examination of uncoated, insulating specimens at higher pressures by utilizing ionized gas to enable automatic discharging, beneficial for studying wet specimens, but with degraded resolution.

2.2 Formation of Secondary Electron (SE) Images

In a scanning electron microscope (SEM), the electron beam, after emanating from the source, traverses along the optic axis of the lens system. It is sequentially refined by apertures and focused via the magnetic and/or electrostatic fields of the lens system. Within the objective lens, a set of scan coils shifts the beam from the optic axis, enabling precise

targeting of the specimen at designated locations. At any given moment, the beam interacts with only a singular location on the specimen.

The SEM constructs images by directing the focused beam across a grid of discrete x - y positions on the specimen and recording the interactions at each point. Typically, this involves collecting signals from an electron detector, such as the Everhart–Thornley detector, which is sensitive to secondary electrons (SEs). Moreover, outputs from multiple detectors can be gathered simultaneously at each beam position, allowing the concurrent construction of multiple grayscale images from different electron signals.

It is important to note that unlike classical optical microscopy, which constructs images through direct ray paths from the specimen to the imaging medium, SEM image formation is inherently digital. Each interaction site is digitized using an analog-to-digital converter (ADC) to convert electron signals into digital data packets (x, y, I_j) , where I_j denotes intensities of various detected signals such as SE, backscattered electrons (BSE), X-rays, etc.

The scanned area is logically divided into an x - y grid of pixels, each with an edge dimension defined by the equation Specimen pixel dimension = $\frac{l}{n}$, where l is the edge length and n is the number of pixels per edge. The beam is systematically positioned at the center of each pixel, where it dwells for a predetermined time to accumulate signal information, which is then stored in a three-dimensional data matrix (x, y, I_j) .

The final SEM image is generated by translating the data matrix into a display grid of pixels, where the brightness of each pixel (varying from black to white) corresponds to the intensity of the measured signals, providing a visual representation of the specimen's surface at microscopic resolution.

2.3 Characteristics of SE Images

Surface Sensitivity

The heightened surface sensitivity of SE imaging arises because only low-energy electrons emitted from the specimen's uppermost layers—typically just a few nanometers deep, are able to escape to be detected. Electrons originating from deeper within the sample lack the energy necessary to reach the surface and be captured as a signal, rendering SE imaging particularly effective for examining the fine details of surface morphology and topography.

Topographical Information

SE images reveal detailed surface topography, including fine features, roughness, and microstructures. They are especially useful for examining the three-dimensional (3D) structure of a specimen's surface.

High Spatial Resolution

SE imaging, with its excellent spatial resolution, enables visualization of surface features with nanometric precision. This is attributed to the confined excitation volume from which SE electrons originate. As SE electrons are produced from interactions in the near-surface region, a shallow excitation volume represented by only the top few nanometers, this limitation naturally enhances the spatial resolution of the SEM. The excitation volume where the SEM scanning we can see in figure 2.2. Such a restricted excitation zone ensures that

the detected electrons contribute to a high-resolution signal that corresponds directly to the fine details of the surface topography.

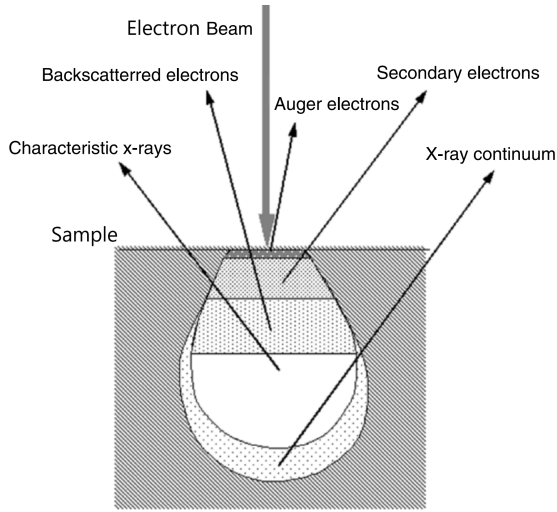


Figure 2.2: Visualization of the material volume sampled through the detection of various signals generated from electron-matter interactions. Adapted from [26].

2.4 Contamination in SEM

Contamination during the scanning electron microscopy (SEM) process poses significant challenges in obtaining high-resolution, clear imagery essential for material characterization and analysis. The following sections delve into the nuances of contamination control, the inherent and extrinsic factors contributing to this pervasive issue, and the methodologies employed to measure and mitigate its impact on SEM operations. Through comprehending the origins, development, and management of contamination, both researchers and practitioners are able to improve the accuracy and dependability of SEM imaging and analysis. This understanding is particularly crucial as advancements in SEM technology continue to push the boundaries of resolution and sensitivity.

Contamination Control in Scanning Electron Microscopy

In scanning electron microscopy (SEM), the term „contamination“ refers to the unintended deposition of foreign materials on the specimen induced by electron beam bombardment. This phenomenon is a particular kind of radiation damage, where the contaminating material, often a hydrocarbon, is present due to the specimen’s environmental history or inadequate sample preparation. These hydrocarbons are susceptible to radiation damage and may decompose under the electron beam, leaving a residual layer of carbon.

Contamination is not only a result of hydrocarbons that were initially on the specimen surface, but it can also be exacerbated by the electron beam-induced migration of these molecules. This leads to an increase in localized contamination, which can impact the quality of SEM imaging and analysis. A modern and well-maintained SEM should produce

minimal contamination from the instrument itself, assuming rigorous attention to cleaning and handling protocols.

To mitigate contamination, it is advantageous for an SEM to be equipped with a vacuum airlock, reducing the specimen chamber's exposure to contaminants during sample exchange. Additionally, a plasma cleaner in the airlock, used during the pump-down cycle, can further reduce contamination by breaking down hydrocarbon deposits. However, care must be taken to prevent potential damage to the specimen from the plasma.

Contamination typically manifests as a change in the secondary electron (SE) yield due to the deposition of carbon-rich material from the electron bombardment. The most significant contamination is often observed at the edges of the scanned area where the electron dose is highest, because of the physical scanning of the beam.

Radiation damage can also have an etch effect, where prolonged electron irradiation removes the material layers, revealing the underlying material with different SE properties. The propensity for contamination is dose-dependent; high-resolution imaging, which requires a highly focused beam and high current density, is more susceptible to contamination issues.

Introduction to contamination in SEM

Electron beam-induced contamination, ie, the deposition of carbonaceous material over the sample surface bombarded by the electron beam, is almost always present after viewing in the scanning electron microscope (SEM). This is one of the most troublesome problems as it induces physical changes in the actual structure of the material being viewed, generally by obscuring the fine detail. Its importance is growing, especially for nanometer resolution imaging, where small surface structures can easily be buried in a few seconds. Therefore, it is essential to find the origins of electron beam-induced contamination, measure it regularly, and keep it at acceptable levels [25].

Sources and types of contamination

Generally, sources of SEM contamination can be attributed to one or a combination of three major contributors: (1) the pumping system (in case the SEM contains oil pumps); (2) outgassing of other internal SEM component parts (ie, specimen stage, stage lubricants, O-rings, etc.), or (3) the sample (including its preparation and handling) [20].

Formation of Contamination Layers

It is critical to understand that the contamination layers depicted in our SEM images are not typical outcomes of standard electron microscope operation. These layers are unusually extensive and are formed under specific conditions that are not commonly encountered during routine SEM usage. The creation of such extensive contamination is primarily due to prolonged exposure of the sample to the electron beam within a confined scanning area under defined image conditions. The particular area selected is placed at the top of the tin ball; see Figure 2.3. The choice of this particular location is due to the spherical shape of the tin ball, which allows the contamination to be clearly visible from the side and provides an optimal condition for measuring its thickness.

This prolonged exposure leads to an accumulation of contamination, which is depicted in Figure 2.4. The electron beam, when stationary or moving slowly over a particular area, induces the deposition of carbonaceous material. Over time, this results in the formation of

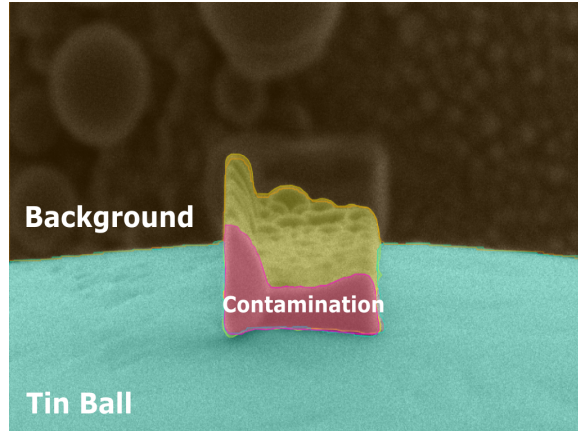


Figure 2.3: Annotated SEM image displaying a contamination layer formed on a tin ball with clearly delineated background and contamination regions.

a visible contamination layer that is much thicker than is usually observed under standard operating conditions. The reason behind this is to quantify the contamination build up over time in the system, to judge its cleanliness.

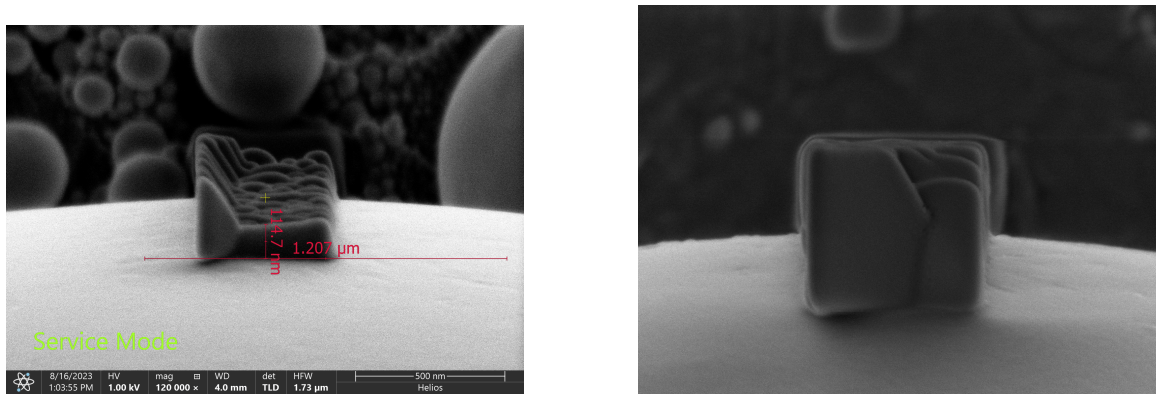


Figure 2.4: Contaminations on the sample surface due to extended electron exposure in SEM. Left: a) contamination of medium size; Right: b) excessively large contamination

Evaluation of chamber contamination in SEM

There are three significant forms of contamination: one is depicted in figure 2.5, where there is minimal contamination, followed by images that show excessive contamination in figure 2.4 b), and then those in figure 2.4 a), in all these images contamination is atop the Tin Ball, with the Tin Balls also apparent in the background. In these images, we can observe both the width and height of the contamination. The width, starting from the bottom of the contamination layer, gives us a sense of how wide it is and is mostly defined by the defined continuous scanning region. The height measurement begins in the middle of the width and extends to the top of the contamination layer, indicating how much contamination has accumulated. The contamination layer exhibits a unique characteristic: a peak on the far left that declines towards the contamination's center after a certain

distance. Specifically, it arises in an area where the scanning beam lingers for an extended period, leading to increased contamination at that spot caused by scanning synchronization. This enhanced contamination is not included in the measurements, and instead, the center of the contamination layer's forefront is used as the reference point for assessments. The measurements obtained are then compared to established thresholds for maximum and optimal contamination levels, which guide our use of the microscope. However, this thesis will not explore these aspects further, as it concentrates on image processing techniques designed to measure and quantify the height of contamination, rather than its creation, preparation, or determining if the contamination level is excessive for the microscope.

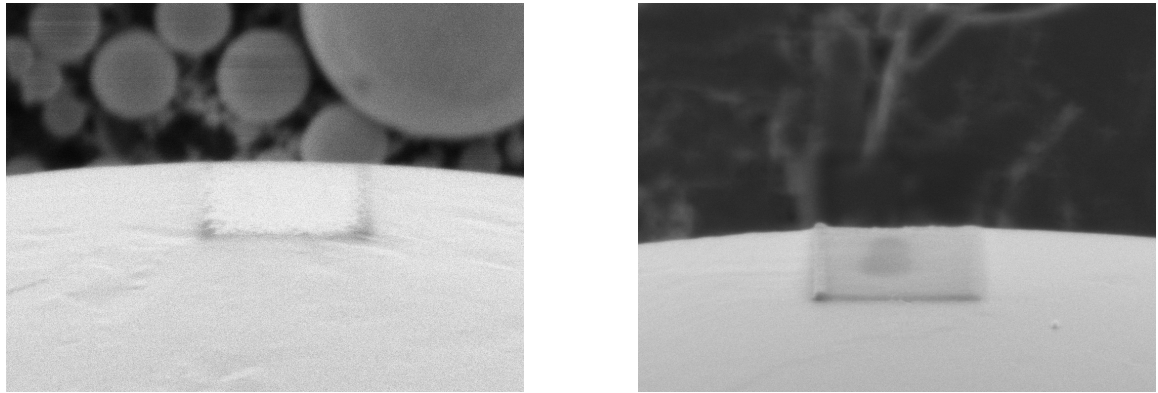


Figure 2.5: SEM images showing a clean sample on the left and slight contamination on the right.

Chapter 3

Measuring Features in SEM Images

This chapter reviews recent advancements in quantifying electron beam-induced carbon contamination in electron microscopes, drawing from the findings of Hugenschmidt et al. [9] and Roediger et al. [22]. These studies provide insight into automated techniques to measure contamination. The subsequent section will discuss methods for image analysis in scanning electron microscopy.

3.1 Measuring Chamber Contamination in SEM

Reproducible Measurement Using Residual Gas Analysis and Electron Beam Deposition

Roediger et al. [22] developed an automated approach that focuses on measuring chamber contamination in scanning electron microscopes through the following methodological steps:

- **Focused Electron Beam Deposition:** By depositing material from the gases onto a substrate under controlled conditions, the study quantifies how much material is deposited over time, which directly correlates to the contamination level.
- **Automated Measurements:** The deposition rate is automatically measured by measuring the thickness of the deposited layer using AFM, which will be discussed in further detail in a further text.

Focused Electron Beam Deposition by depositing material from these gases onto a substrate under controlled conditions, the study quantifies how much material is deposited over time, which directly correlates to the contamination level and then measuring the thickness of the deposited layer. This approach allows for continuous monitoring of contamination levels in the SEM chamber and provides data that can be used to optimize chamber cleaning schedules and other preventive maintenance strategies. It is necessary to mention that this work is using for analysis and quantification of contamination separate atomic force microscope. It was used in tapping mode. The tapping mode means that as the tip scans across the sample surface, it intermittently taps or lightly contacts the surface. This tapping interaction provides information about the sample's surface topography and mechanical properties of the sample.

Electron-Beam-Induced Carbon Contamination in STEM-in-SEM

The study by Hugenschmidt et al. [9] shows that STEM-specific technologies, such as High Angular Annular Dark Field (HAADF), provide exceptional capabilities for measuring contamination through visualization of high-contrast images directly related to the atomic number of elements. However, these advanced techniques require the transmission of electrons through very thin specimens, a requirement that is not applicable in traditional SEM setups where the electron beam interacts primarily with the surface.

Conclusion

Although the studies by Hugenschmidt et al. [9] and Roediger et al. [22] are instrumental in advancing contamination measurement within electron microscopy, their application to STEM-in-SEM platforms specifically highlights the unique challenges faced in adapting SEM technologies for contamination analysis. This discussion underscores the need for SEM-specific techniques for measuring contamination, as SEM does not involve electron transmission through the sample, making STEM techniques like HAADF inapplicable and the use of atomic force microscopes is not applicable either. There appears to be no existing work that implements automatic contamination measurement under SEM conditions, as described in our methods, which rely on detecting the contamination layer formed at the edge of a tin ball.

Unlike other methods, which use different metrics for contamination quantification, our approach focuses on the visible side layer created by electron bombarding on the edge of the round tin ball. To my best knowledge, there are no studies on measuring contamination under these specific conditions using automatic methods. Subsequent studies will concentrate on SEM image analysis related to contamination assessment and explore image processing techniques that could aid our objectives, leading to the development of novel methods appropriate for measuring contamination layer.

3.2 Image Analysis for Contamination Assessment

This section delves into the utilization of diverse image processing techniques suitable for assessing contamination in SEM. Our goal is to find the technologies used for measuring layer heights in images or in detecting the features. Consequently, this section will examine the image analysis methods related to similar issues in electron microscopy.

Electron microscopy is widely used across various fields such as drug discovery, structural biology, cell biology, infectious diseases, cancer, plant biology, and semiconductors. Each of these areas has seen substantial research and development. However, our focus on contamination measurement introduces a distinct challenge not commonly addressed in the literature. Although there are studies, few align closely with our specific needs. For this purpose, our attention is directed towards exploring studies on image analysis techniques, which will be employed in the following chapter to outline our two proposed methods, discussed further in chapter 4.

Morphological Operations for Thin Film Analysis

The research conducted by Su Junhong, Ge Jinman, and Yang Lihong [23] enhanced the precision and efficiency of measuring thin film thickness, a crucial element in materials science. This research played a key role in integrating morphological operations into the assessment of thin film parameters obtained through interferometry. It is important to note that this research does not rely on SEM, yet it focuses on image preparation for thin film thickness measurement. Morphological operations, play a pivotal role in the preprocessing and enhancement of digital images. In the context of thin film thickness measurement, these operations are crucial for improving the quality and accuracy of the data extracted from interferograms. Su Junhong et al. have effectively employed morphological techniques such as erosion, dilation, opening, and closing to address various image artifacts. Specifically, the use of structured elements tailored to the unique characteristics of the interferogram noise and thin film edges facilitates a more precise delineation and recognition of the film's boundaries. This is crucial for accurate thickness measurement as it directly impacts the subsequent computational steps in edge detection. In our scenario, we face a comparable task initially with the images where our aim is to normalize the images and eliminate any artifacts that could potentially compromise our measurements.

Otsu Thresholding

Otsu's method, developed by Nobuyuki Otsu in 1979 [18], is a thresholding technique pivotal in the field of image processing for its efficacy in segmenting images into foreground and background. This method determines an optimal threshold by maximizing the inter-class variance, thus facilitating the clear distinction between different components in grayscale images. Traditionally, Otsu thresholding has been broadly applied across various scientific and industrial domains, particularly where binary segmentation of images is crucial. Its algorithm involves analyzing the histogram of pixel intensities and calculating a threshold that segregates pixels to minimize intra-class variance, equivalent to maximizing the inter-class variance. This characteristic makes it particularly useful in applications ranging from medical imaging to automated industrial inspection.

In the study of Si/C–Graphite composite anode microstructure using focused ion beam scanning electron microscopy (FIB-SEM) [11], Otsu thresholding has been instrumental. The technique has been adapted to enhance the precision in analyzing the subtle contrasts and intricate details typical in FIB-SEM images of battery materials. Researchers integrated Otsu thresholding with advanced preprocessing techniques, such as noise reduction and contrast enhancement, to address specific imaging challenges like curtain artifacts and non-uniform illumination. The workflow developed in the referenced study extends the basic application of Otsu's method by incorporating it into a systematic algorithm that includes both pre- and post-processing stages designed to refine the segmentation process. This integrated approach is critical for achieving high segmentation accuracy necessary for reconstructing the three-dimensional structure of the anode and assessing its electrochemical performance and serves as a prime illustration of how combining preprocessing methods with the thresholding technique can maximize the benefits derived from otsu thresholding. The effective use of Otsu thresholding in this research not only demonstrates its robustness but also its adaptability to complex imaging scenarios. By combining Otsu's method with other image processing techniques, the researchers enhanced its utility, making it an invaluable tool in the detailed analysis of electrode materials for lithium-ion batteries. Otsu's method applies thresholding to distinguish between foreground and background, which is

similar to the scenario in our SEM contamination images. In these images, the foreground features a whitish tin ball with a darker contamination layer, while the background appears blackish and includes several smaller tin balls.

Edge detection and Region of Interest

Edge detection is a fundamental component in image processing and a critical step for feature extraction in the field of computer vision. It aims to identify points or regions with significant changes in brightness or intensity, which often correspond to edges within the image.

In SEM imaging study, Sun et al. [24] discuss the efficacy of traditional edge detection algorithms, including Sobel, Laplacian, and Canny operators, which are typically used to identify image boundaries through variations in grayscale gradients. The study evaluates these techniques on multilayer thin film images, determining that the Canny operator excels in both accuracy and computational efficiency for their specific application. In addition, this work proposed an edge detection method based on mask operation to enhance the clarity of edges in SEM images of multilayer thin film materials. Manual mask selection is not applicable in our context; however, their extensive utilization of regions of interest is noteworthy and warrants consideration for the development of robust methods in our case. We could attempt to locate the contaminated area and subsequently focus all edge detection efforts solely within that region of the image. Despite these advancements, edge detection in SEM images remains a challenging task due to its inherent noise and complex structures.

Cut-face Edge Detection

Kutálek's approach [13] tackles the challenge of edge detection in SEM images used to assess the thickness of material layers that have been removed from a sample, which closely parallels our scenario of measuring layers that have been added instead. It is done by converting a two-dimensional image slice into a one-dimensional vector. This transformation is performed by first averaging the pixel intensities throughout the image and then applying a moving average for further smoothing. The core of this method is the subsequent convolution with a Gaussian window, which greatly improves the precision of edge detection. Initially, transforming 2D image data into a 1D vector of averaged pixel intensities streamlines the complex data, facilitating easier handling and analysis. The use of a moving average enhances this transformation, highlighting variations in intensity to more clearly expose hidden patterns. Convolution with a Gaussian window accentuates the identified edges, making them more distinct and easier to recognize.

Deep Learning Approaches

In the study from Liu et al. [14], semantic segmentation has become a transformative approach in biomedical image analysis, enabling precise delineation and quantification of cellular structures like mitochondria from imaging datasets. The transition from conventional thresholding methods to sophisticated deep learning models has markedly enhanced both the precision and speed of segmenting mitochondria.

Additionally, „Deep Learning, Feature Learning, and Clustering Analysis for SEM Image Classification“ by Aversa et al. [1] further demonstrates the utility of deep learning, particularly CNNs, in enhancing the classification of nanoscale structures within SEM images.

This exploration of the integration of supervised and unsupervised learning underscores the adaptability of deep learning in addressing the challenges posed by the variability of SEM images. In this study, they also analyzed the training of the dataset for classification from scratch across various architectures as well as the fine-tuning process. They discovered that fine-tuning not only accelerated the process compared to initiating from scratch but also improved test accuracy, establishing it as a superior method.

There is a semantic segmentation architecture that is used several times, which is called DeepLabv3 [4]. For instance, in the work „MudrockNet: Semantic segmentation of mudrock SEM images through deep learning“ by Bihany et al. [2] created his own net based on the DeepLabv3 architecture. The model addresses the specific challenges posed by the SEM images of mudrock, such as the presence of silt and clay grains alongside the pores, all with overlapping grayscale values. This advancement specifically, the segmentation of individual pores and grains in mudrock SEM images is crucial for enhancing the understanding of their petrophysical properties, which are pivotal in sectors like petroleum exploration and anthropogenic waste sequestration. In addition to the uses of the DeepLabv3 architecture in various domains, it has also been successfully applied to the segmentation of minerals in reflected light microscopy images. A recent study employs the DeepLabv3 model to address the challenging task of differentiating between opaque and non-opaque minerals from epoxy resin. This method has shown remarkable segmentation accuracy, particularly benefiting from modifications to the original architecture that enhance detail recognition at the borders of mineral particles [6]. These advancements in semantic segmentation model demonstrate significant potential for improving the efficiency and accuracy of mineral characterization processes in the mining industry.

To conclude, deep learning proves to be highly effective in image analysis across biomedical, materials science, and other related disciplines. Studies by Liu et al. and Aversa et al. demonstrate improvements in segmentation and classification accuracy. Furthermore, the adaptation and refinement of DeepLabv3 architectures in specialized applications, as shown by Bihany et al., highlight the potential of these techniques to tackle complex segmentation challenges like ours with high precision and efficiency. It is essential to note that this discussion merely scratches the surface of applying deep learning in SEM, with numerous studies still to be explored. In the following section 3.2, we will explore in detail the study by Minhas on „Transfer Learning for Segmentation Using DeepLabv3 in PyTorch“ [15], which is directly relevant to our problem and also gains advantages from avoiding training from the beginning, as recommended in work by Aversa et al. [1].

DeepLabv3-Based Image Segmentation

Upon reviewing image analysis applications in SEM, we encountered a study unrelated to SEM yet involving a similar task. To address the challenge of feature measurement under the constraints of limited data, in particular the study by Manpreet Singh Minhas on „Transfer Learning for Segmentation Using DeepLabv3 in PyTorch“ presents a compelling methodology leveraging transfer learning with DeepLabv3 for road crack detection [15]. This approach exemplifies the potential of transfer learning in improving the accuracy of segmentation tasks in SEM image analysis, even with sparse datasets.

Background and Methodology The essence of transfer learning, as explored by Minhas [15], lies in adapting a pre-trained model to a new, but related, task. DeepLabv3 [4], a model developed by Google and pre-trained on a large dataset, is utilized for the semantic

segmentation of road cracks from a relatively small dataset of just 118 images. The procedure involves fine-tuning DeepLabv3’s segmentation sub-network to cater to the specific requirements of the new dataset, a process significantly less resource-intensive than training a model from scratch.

Adapting DeepLabv3 for Custom Datasets Modifications to the DeepLabv3 model were necessary to tailor it to the target task of road crack detection. The core adaptation involved altering the output channels of the model’s classifier to match the number of target categories in the dataset with road cracks. This adjustment is crucial for the model to accurately learn and predict the segmentation masks corresponding to road cracks.

Performance and Adaptability The resilience and flexibility of DeepLabv3 in the face of image degradations such as noise and blurring have been rigorously evaluated by Christoph Kamann and Carsten Rother. Their research highlights the model’s capability to maintain high accuracy even when subjected to distortions similar to those encountered in SEM image segmentation [10]. The study implies that enhancements in the model’s robustness are directly linked to its improved performance, a critical factor for dependable SEM image analysis.

3.3 Conclusion

This section highlights the necessity of developing innovative methods to assess contamination in the SEM industry. We aim to devise techniques that diverge from the existing approaches applied in various SEM fields. Although the SEM industry is extensive and has seen significant research, there is a gap in specific studies on automated contamination quantification. Our goal is to develop innovative techniques and evaluate their precision with our own datasets, setting the error margin in nanometers for these measurement methods. This chapter discusses potential solutions to issues akin to ours and establishes a foundation for the innovative methods proposed in the following chapter 4 to measure contamination in SEM.

Chapter 4

Proposed Methods for Measuring Contamination Layer Thickness

This chapter presents two techniques for assessing the thickness of contamination layers in Scanning Electron Microscopy (SEM) images. The initial technique focuses on cut-face edge detection [13], which utilizes image processing and incorporates established pre-processing and thresholding methods to identify regions of interest, and the second involves fine-tuning the DeepLabv3 [4] model, a machine learning approach, for precise contamination segmentation.

4.1 Evaluation of Existing Methods and The Need for New Approaches

This section explores the limitations of measuring the thickness of the contamination layer in SEM images, highlighting the need for specialized approaches tailored to the intricacies of SEM contamination analysis.

Limitations of the Cut-Face Technique

The cut-face technique, while robust for significant pixel value changes, confronts limitations in the nuanced context of SEM contamination measurement:

- **Inconsistent Contamination Presentation:** Contamination can manifest anywhere on the tin ball, without the uniform position required for the cut-face technique, complicating its application.
- **Variable Transition Zones:** Transition zones, especially at the top of the contamination layer, may not exhibit the pronounced changes in the pixel value on which the cut-face technique is based, leading to measurement inaccuracies.

Limitations of Semantic Segmentation Challenges

Semantic segmentation models face their own set of challenges in adapting to the variability present in SEM contamination images:

- **Challenges in Model Training with Diverse Contamination Patterns:** The model's training on datasets, such as those focusing on crack detection showed in

work by Minhas [15], where variability is primarily in crack positioning against a consistent background, contrasts sharply with the nature of SEM contamination images. In contamination analysis, each image can significantly differ in terms of both the material properties and the contamination characteristics, presenting a unique challenge. Finetuning a model to accurately detect contamination across such a diverse set of images, especially with a limited dataset, poses significant difficulties.

- **Lack of Specialized Datasets:** The absence of a dedicated and annotated dataset for SEM contamination layers complicates the training and effectiveness of semantic segmentation models for this specific application.
- **Lack of automation mask threshold finder:** When the model is fine-tuned and applied to an image, it produces a probability mask. This mask must be thresholded at a certain probability value. However, there is no automatic tool available to establish this threshold value to my best knowledge.

4.2 Proposed Methods

Both methods are here described very briefly the detailed chapter dedicated to both methods is 6.

4.2.1 Edge Detection-Based Contamination Analyzer (EDCA)

The Edge Detection-Based Contamination Analyzer (EDCA) utilizes an algorithm adapted from the cut-face technique to enhance contamination detection and edge delineation in SEM (Scanning Electron Microscopy) images. The approach begins by pre-processing images to rectify artifacts using morphological techniques, thereby enhancing the visibility of edges through the use of Otsu thresholding and blurring. The core of EDCA involves applying edge detection filters, to precisely identify contamination edges against the SEM background. These identified edges define the region of interest (ROI), which is crucial to isolate contaminated areas for focused analysis. Subsequent steps include analysis to detect significant edge contours and thickness measurement of the contamination layer by quantifying the pixel distance between edges within the ROI based on cut-face. Calibration with known scales converts these measurements from pixels to precise nanometric dimensions. Detailed implementation steps will be discussed in Section 6.1.

4.2.2 DeepLabv3-based Contamination Layer Segmentation

The refinement of DeepLabv3 is centered on tailoring this advanced deep learning architecture to accurately detect and delineate contamination layers in SEM imagery. Initially, the process involves assembling a detailed dataset of labeled SEM images that display a variety of contamination scenarios, as discussed in sections 5.1 and 5.2. This dataset is subsequently utilized to refine the DeepLabv3 model as described in 6.2. After training, the model is capable of segmenting new SEM images, offering detailed pixel-level classifications that help to measure the thickness of contamination through segmentation masks. To boost the model's robustness, the dataset includes artificially altered images that mimic various imaging conditions, as explained in 5.4. Additionally, an automated script adjusts the threshold settings for the model's output probability maps, detailed in 5.5.

Chapter 5

Data Collection and Analysis

This chapter offers an in-depth explanation of the systematic gathering, preparation, and manipulation of images to establish a sturdy dataset that can support complex analyses. It outlines the incorporation of automated scripts that ensure that each image uniquely illustrates the contamination layers devoid of irrelevant information. In addition, the chapter expands on the stringent procedure of constructing a carefully annotated dataset, which acts as a foundation for the creation and evaluation of machine learning models that automate the partitioning and comprehensive analysis of these images.

5.1 Data Collection

This section describes the methods used to build a dataset suitable for accurately analyzing contamination layers. The dataset consists of two main parts: an initial subset with images lacking dimensional marks and a larger subset predominantly showcasing images with various dimensional marks, including both colorful and grayscale representations; see figure 5.1. The two datasets were supplied by Thermo Fisher Scientific and consist of contamination measurements conducted manually by experts over the past few years.

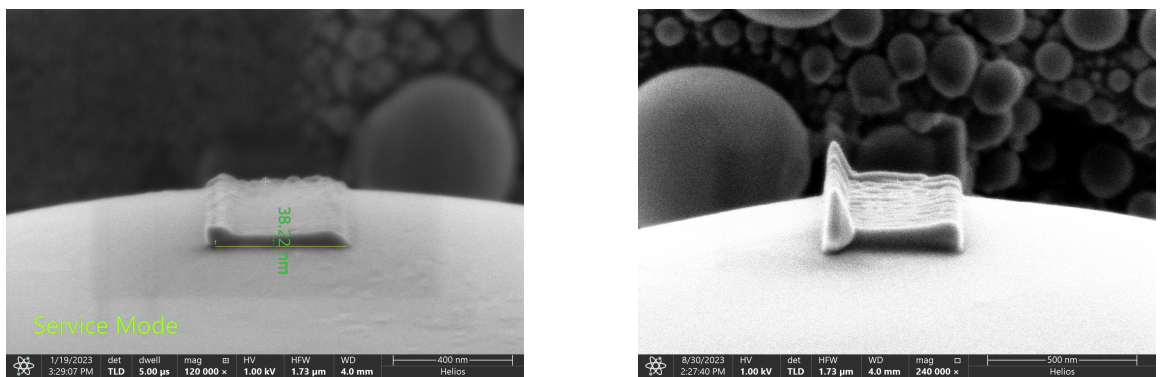


Figure 5.1: Dataset samples showcasing a specimen adorned with noticeable dimensional marks on the left and without the dimensions on the right. For both the lower section of the image contains important details outlining the settings employed for capturing the image through electron microscopy.

Removing bottom information bar

The dataset initially contained images that encompassed extraneous elements at the bottom, particularly service information and data used for measurement. To refine these images, a tailored cropping approach was employed. The script systematically analyzed the image dimensions and selectively cropped sections based on a pre-defined mapping of the image sizes. This mapping allowed for the removal of unnecessary lower sections from the images with the text „Service Mode“, thereby creating a cleaner dataset optimized for contamination layer analysis.

Dimension Removal Process

This section discusses the implementation of image processing methods aimed at the elimination of dimensional annotations and markings from images. To incorporate these images into our dataset for evaluation and fine-tuning purposes.

Color-Based Masking

Initialize an object to manage the dataset and set specific color ranges to identify regions representing dimensional markings within the images. A pivotal technique involves color-based masking. This process involves transforming the images from the conventional RGB color space to the HSV (Hue, Saturation, Value) color space. By defining specific ranges of HSV values, masks are created to isolate areas of interest corresponding to the colors associated with dimensional annotations; see Figure 5.2.

These masks highlight the regions containing the markings, enabling them to differentiate them from the rest of the image content. To refine the areas detected, a morphological operation *dilation* is applied to the masks. This operation expands the marked regions, helping to cover all-dimensional annotations effectively.

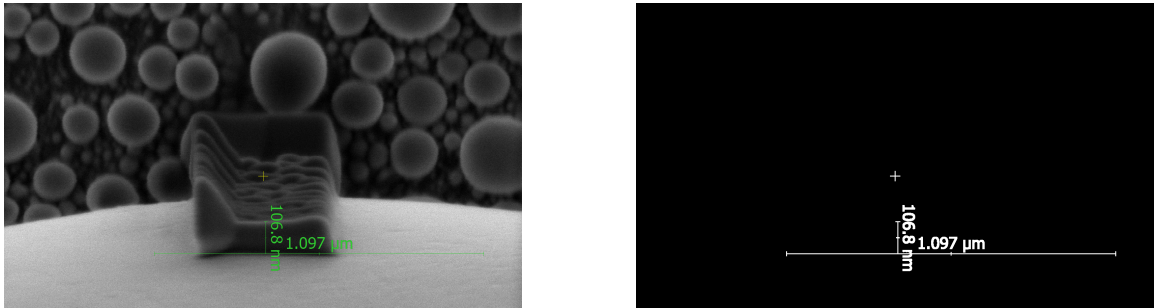


Figure 5.2: Left: Pre-masked image with dimensional annotations clearly visible in green. Right: Resulting mask highlighting these annotations, prepared for further processing steps.

Inpainting for Markings Removal

Once regions with dimensional markings are identified using the combined mask, they undergo a technique called „inpainting“. This method reconstructs the marked areas by utilizing information from the adjacent unmarked regions, following the Navier-Stokes algorithm [5]. As a result, the dimensional annotations are effectively removed, producing

a clean and unmarked representation of the original content, as illustrated in the result Figure right 5.3.

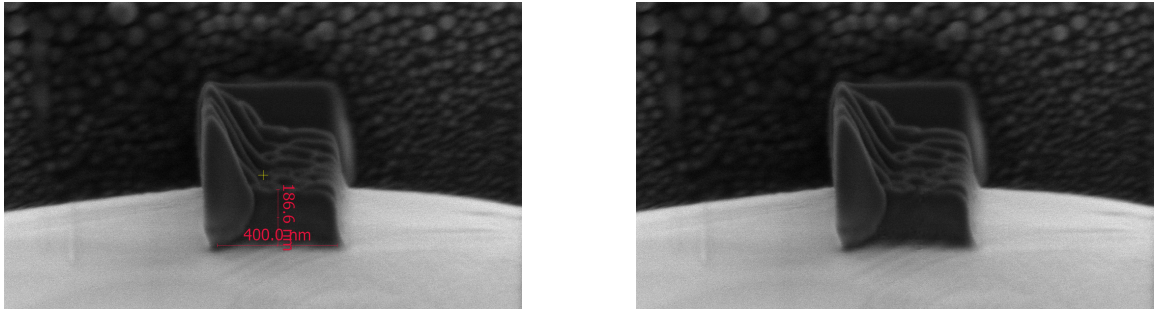


Figure 5.3: Left: Original image with dimensional markings used for measurement. Right: Image after application of inpainting techniques, where dimensional markings have been removed.

5.2 Annotation Dataset and Automatic Tests

This section discusses the development of an annotation dataset and the implementation of automated tests to validate the image processing methods used in this study.

Annotation Dataset Creation

The labeling of SEM images is a meticulous process that involves identifying unique characteristics in each image, such as contamination layers. Consequently, a SEM image dataset was created with particular attention to the following requirements:

- **Annotation Process:** 654 images from the dataset were annotated by hand. This process involved identifying contamination and storing the annotated masks in a designated folder. The naming convention of this folder corresponds to the original images, simplifying subsequent tasks such as error calculation, validation, and model refinement.
- **Quality Assurance:** Every image that was annotated underwent a verification process to confirm the correctness of the labels compared to actual measurements taken from images that were annotated with dimensions prior to their removal.

Created Datasets

We have developed a total of four datasets from all our obtained images. These datasets are divided into two categories: one featuring contamination and the other encompassing both contamination and no contamination, as initially illustrated in the types of contamination in images at the beginning 2.5 and 2.4. Two versions of these datasets exist, one designed for fine-tuning and the other for validation purposes. These will be further explored in relation to evaluating the model's effectiveness as outlined in the chapter 7. The datasets were separated to facilitate experiments with fine-tuning the model on one of these datasets because we aim to determine which model will deliver superior results and reliably detect any contamination in the images.

- **Contamination_Only_Dataset** - Contains 339 contamination images.
- **Default_Dataset** - Contains **Contamination_Only_Dataset** and zero contamination images. This dataset is obtaining 563 images.
- **Uniq_Contamination_Only_Dataset** - Contains 54 contamination images. This dataset is created only to validate how the models perform and to compare them between each other.
- **Uniq_Dataset** - Contains **Uniq_Contamination_Only_Dataset** and zero contamination images. It is also used same as the previous dataset for models. This dataset is obtaining 91 images.

These annotated images serve as the ground truth for fine-tuning and evaluating the performance of both implemented methods designed to automatically measure contamination in SEM images.

5.3 Automated Testing of Image Analysis Algorithms

Automating the measurement of contamination in SEM images facilitates the evaluation of the performance of each method throughout its implementation and testing phases. The provided Python script is designed to identify and quantify contamination areas, which are represented by other than black regions in the processed SEM images shown in figure 5.4. The following subsections describe the functionality and workflow implemented in the script. It is essential to note that this algorithm, which measures height from the mask, is similarly applied to assess thickness in the fine-tuned model's output mask after the thresholding of the probability map.

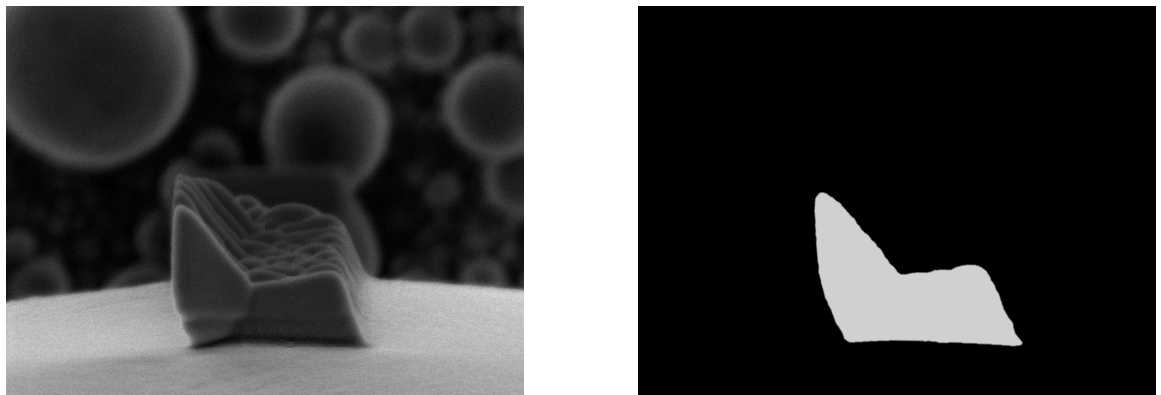


Figure 5.4: Left: SEM image displaying contamination layer. Right: Corresponding mask highlighting the front side of contamination layer.

Measuring Height in Images from Mask

For every manually annotated mask, the function computes the height of the area within a column, which is precisely in the center of the width of the mask:

1. The image is loaded and thresholded to filter out all colors except black, thereby isolating areas of contamination. Subsequently, it detects the contours of these areas.
2. Identify the furthest left and right points of the mask, which will determine the central column where the height measurement will be taken.
3. Searches vertically through the specified column to locate the top- and bottom-most other than black pixels.
4. The vertical distance between these two points gives the height of the measured area.

Data Collection and CSV File Generation

The main execution block of the script performs the following steps:

1. Defines the directory containing the images and initializes the CSV file to store the results with headers.
2. Iteratively processes each image in the directory, applying the width and height measurement functions to determine the dimensions of contamination.
3. Outputs the measured values and writes them to the CSV file, associating each measurement with the corresponding image file name; see Table 5.1.

The dataset captured in the resulting CSV file organizes each image's analysis into the following format:

- **ImageName:** The file name of the analyzed SEM image.
- **BottomHeightY:** The distance in pixels from the top of the image to the lowest point of the contamination region.
- **TopHeightY:** The distance in pixels from the top of the image to the highest point of the contamination region.
- **ContaminationHeight:** Vertical span in pixels of the contamination region.

Extensibility of the Automated Measurement Integration

The script's design naturally supports the dynamic addition of new images and their associated measurement values to the CSV file. This functionality underscores the utility of the script, as it allows for the seamless integration of fresh data, thus continuously enriching the dataset. This feature is pivotal for maintaining an up-to-date repository, making it ideal for iterative analysis and automated testing that evolves with the addition of new images and subsequent contamination measurements.

5.4 Data Augmentation

Data augmentation plays an essential role in training machine learning models, especially for tasks that require a high generalization in diverse input scenarios, such as SEM image segmentation. Our augmentation strategy is designed not only to increase the diversity

| ImageName | BottomHeightY | TopHeightY | ContaminationHeight |
|--------------------|---------------|------------|---------------------|
| H6EX10_S_..._1.png | 544 | 633 | 89 |
| H6EX12_S_..._1.png | 565 | 587 | 22 |
| H6EX12_S_..._1.png | 567 | 600 | 33 |
| H6EX17_S_..._1.png | 583 | 684 | 101 |
| H6EX17_S_..._2.png | 567 | 641 | 74 |
| H6EX17_S_..._3.png | 500 | 585 | 85 |
| H6EX20_S_..._1.png | 572 | 594 | 22 |
| H6EX20_S_..._2.png | 556 | 582 | 26 |
| H6EX20_S_..._1.png | 541 | 670 | 129 |
| H6EX20_S_..._2.png | 431 | 579 | 148 |

Table 5.1: This table presents a portion of the dataset, illustrating the automated measurement of contamination heights in SEM images. Detailed are the positions of the bottom and top height positions, alongside the calculated contamination height for a selection of samples.

of the training dataset but also to ensure that key geometric properties of contamination, specifically the perpendicular orientation of start and end lines, are maintained. This section elaborates on the augmentation methods used, utilizing the Python library Albu-
mentations [3].

Augmentation Pipeline

The augmentation pipeline is carefully constructed to apply transformations that simulate realistic variations in SEM imaging conditions without distorting critical contamination characteristics see results in Figure 5.5. Here are the specific transformations used:

- **Noise and Blur:** This transformation introduces Gaussian noise with a variance between 10.0 and 50.0 to mimic SEM image artifacts, applied with a 70% probability. Additionally, blur and median blur with a limit of 3 simulate focus variations, included in a composite operation under the `OneOf` clause, each with an individual application probability of 100%, but collectively with a 70% probability due to the parent setting.
- **Elastic Transformations:** The use of `ShiftScaleRotate` without rotation simulates minor elastic-like deformations through controlled shifts (`shift_limit=0.0625`) and scales (`scale_limit=0.1`), ensuring that critical contamination boundaries remain aligned and undistorted.
- **Brightness and Contrast:** Random adjustments in brightness and contrast are applied with limits of 0.2 to account for variations in illumination conditions and sensor sensitivity across different SEM machines. These adjustments are also set with a 70% probability of application.
- **Scaling and Translation:** The pipeline includes random scaling (limited to 0.1) and translation (shift limit set to 0.0625) without any rotation, ensuring the orientation and perpendicularity of contamination lines are maintained, crucial for accurate SEM image analysis.
- **Additional Details:** All images are resized to 320x480, standardizing the input size for subsequent model fine-tuning. Each transformation is applied ensuring that

the same modifications are mirrored on both the image and its corresponding mask, preserving the alignment between the two.

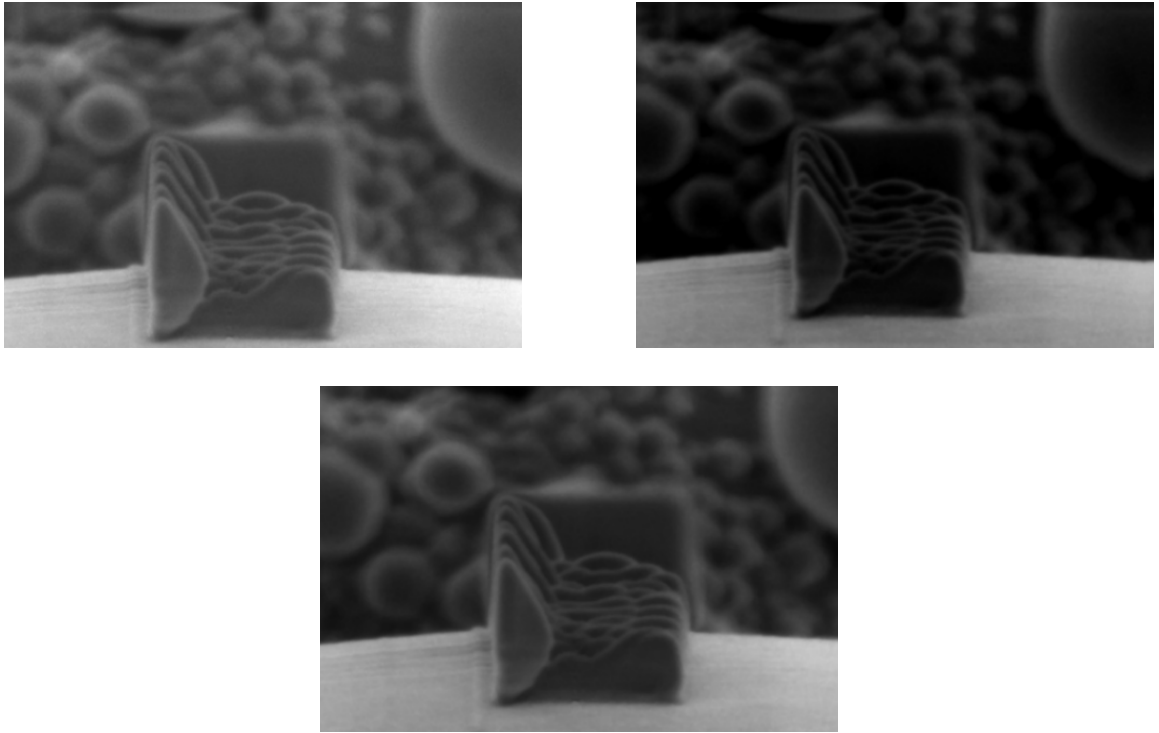


Figure 5.5: Examples of data augmentation techniques applied to one SEM image. The images demonstrate the application of various transformations.

Implementation of Augmentation

The augmentation process is implemented using a multiprocessing approach to efficiently handle a large dataset and significantly speed up the processing time. Each image and its mask undergo the defined transformations, and the augmented results are saved into specified directories for subsequent training usage. The process is described in the provided Python script, which reads images and masks from specified directories, applies the augmentation pipeline, and writes the output to new directories.

Preservation of Perpendicular Lines

Special attention is given to ensure that the start and end lines of contamination, which are critical for accurate measurement and classification, remain perpendicular after augmentation. This is achieved by carefully calibrating the elastic and affine transformation parameters within the Albumentations library to avoid any rotational effects that might tilt these lines.

This strategic approach to data augmentation ensures that the augmented images faithfully represent possible real-world scenarios while maintaining the integrity of critical structural information in the SEM images.

5.5 Automation Mask Threshold Finder

In this section, we discuss the development of a Python script specifically designed to accurately determine the optimal threshold value for a probability map. This task is essential to improve the accuracy of the model in applications that rely on probability-based segmentation.

Motivation

The choice of threshold value for interpreting probability maps significantly affects both the accuracy of predictive models and the precision of error measurements used in subsequent validation steps. An optimally chosen threshold ensures that the probability maps effectively distinguish between areas of front contamination layer and background, thus minimizing false positives and negatives.

Implementation

Input: The input to our process is a probability map, as depicted in Figure 5.6.

Output: The output is a binary mask, highlighting regions where the probability value exceeds the found threshold.

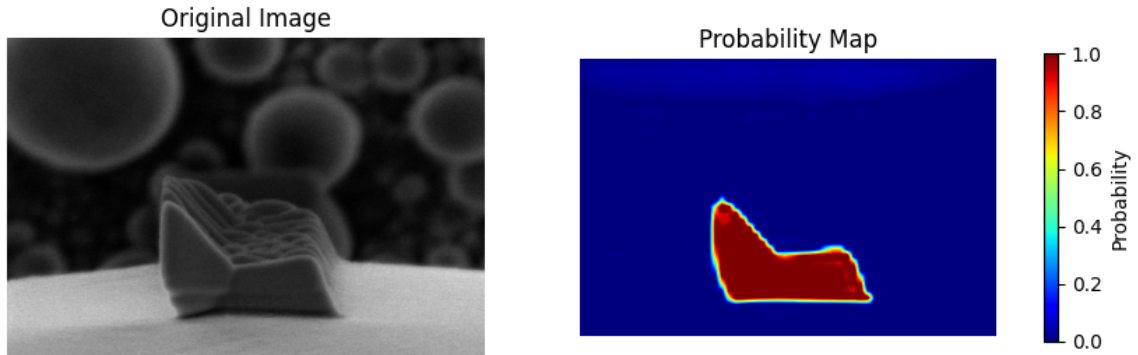


Figure 5.6: The left side presents the original image, while on the right, the resultant probability map is shown, which has been derived through the application of the model to the original image.

Data Preparation

Our dataset comprises all available images, each labeled with height, the Y position top and the Y position bottom. These annotated data form the basis for comparing the results produced by different threshold values.

Initial Parameter Setup

- **Minimum Threshold:** Set to 0.
- **Maximum Threshold:** Set to 1.
- **Threshold Step:** Initially set to 0.025.

Optimization Loop

This stage is crucial to refine the threshold value to ensure the highest possible accuracy. The process involves a series of iterative adjustments based on the errors computed for each threshold value.

1. **Initial Assessment:** Review each image in the data set and apply the model-generated probability map using a threshold mask. This mask helps to measure the bottom, top, and height of the front contamination layer, capturing these values in a dictionary for subsequent error analysis.
2. **Compute Error Measurement:** Calculate the mean error for each image in the dictionary tested. This involves averaging the absolute differences in height, top Y position, and bottom Y position for each image compared to its annotations stored in CSV as mentioned in the previous section about annotation dataset [5.2](#).
3. **Threshold Adjustment:** Increment the threshold value by the predefined threshold step and revert to the initial assessment phase. If the threshold surpasses the maximum value, we proceed to the subsequent steps outlined below.
4. **Identify Optimal Range:** Determine the threshold value that results in the smallest average error by summing up the top and bottom errors of each threshold value computed in the initial 3 stages, and then select the one with the smallest value as the most suitable threshold value. This threshold signifies the most precise distinction. This threshold indicates the most accurate separation between relevant and irrelevant regions in the probability map. If the threshold step falls below the established precision accuracy value, then the script is terminated using the threshold value found in this iteration as the ideal threshold mask value.
5. **Refine Threshold Step:** Once the threshold with the minimum sum error is found, the threshold step is halved. This refinement increases the precision of the threshold values tested in subsequent iterations.
6. **Adjust Search Bounds:** To enhance efficiency and focus computational resources:
 - **Update Minimum Threshold:** Set the new minimum threshold to the best performing threshold minus five times the new (halved) threshold step. We have empirically found that using five times the threshold step optimizes our search bounds effectively.
 - **Update Maximum Threshold:** Set the new maximum threshold to the best-performing threshold plus five times the new threshold step. This adjustment has been empirically determined to work best for our applications.
7. **Repeat Process:** Continue the evaluation process with the updated threshold settings, beginning anew from the Initial Assessment. This cycle persists until the threshold step decreases below the set precision value. In our particular scenario, the precision is established at 0.005. This ensures a comprehensive evaluation of potential threshold values within the most promising range.

Results Compilation and Storage

The iterative process of refining the threshold value not only narrows down the range of possible thresholds, but also incrementally enhances the precision of image segmentation. By systematically reducing the threshold interval and judiciously adjusting the limits, this method significantly accelerates the identification of the optimal threshold, thereby decreasing computational demands while sustaining or heightening the accuracy of the results. Concurrently, after each iteration, error metrics for each threshold are meticulously stored in a CSV file for subsequent analysis and verification of the threshold determination process. This deliberate and efficient strategy sharpens the focus on the most viable threshold ranges, fostering a faster attainment of the best solution and ensuring the dependability and consistency of the segmentation outcomes.

Chapter 6

Implementation of Proposed Methods

In this chapter, we explore the implementation of the Edge Detection-Based Contamination Analyzer (EDCA). Subsequently, we examine an enhanced method that employs the DeepLabv3 model, designed specifically for the segmentation of contamination layers in SEM images. This section investigates the intricacies of training a specialized deep learning model, its configuration, and the comprehensive training cycle. Each technique is thoroughly described, with insight into the technical execution. Research techniques and methods have been enhanced by insights derived from the book „Digital Image Processing“ [8], which has been instrumental in refining our approach to image analysis and processing.

6.1 Method 1: Edge Detection-Based Contamination Analyzer (EDCA)

Image Preprocessing

Inspired by the work of Su Junhong et al. [23], we adopt a series of preprocessing techniques specifically tailored to optimize the input images for edge detection algorithms. Given the significant variability among images, normalization of the input for the method was essential.

- **Morphological Operations (Opening and Closing):** Morphological operations are employed, starting with an Opening operation, which is beneficial for eliminating small objects or noise in the image foreground while retaining the shape and size of larger objects. This is followed by a Closing operation, essentially the antithesis of opening, involving dilation followed by erosion. These processes aim to seal minor holes or gaps within foreground objects, smooth edges, fill in small holes, or bridge nearby objects separated by small gaps. These steps are instrumental in removing minor specks of noise or artifacts and ensuring that the contamination is not obscured by such disruptions.
- **Noise Reduction and Detail Minimization:** We apply then noise reduction technique Gaussian Blurring to diminish image noise and detail by weighted averaging the pixels within a 11 kernel-sized window. This technique is suitable for reducing

noise and minimizing details, facilitating enhanced performance in subsequent tasks like edge detection by rendering edges smoother and less fragmented by noise.

Edge Detection

Edge detection using the Scharr operator is employed solely to identify regions of interest due to inconsistency over the data. The edge detection phase leverages established edge detection techniques to identify potential boundaries between the contamination layer and the background. The following steps constitute the edge detection process:

- **Thresholding (Otsu’s Method):** Utilizing Otsu’s thresholding technique [18], the image will be segmented into foreground and background regions by employing optimal thresholding values derived from the image histogram. This approach is particularly well-suited for the given scenario, considering the presence of a large tin ball and the background behind it; see Figure 6.1.
- **Scharr Edge Detection:** Referencing findings from a study [16], which highlighted the efficacy of both the Canny and Scharr edge detectors, we undertook testing on our SEM dataset. These tests confirmed that while both methods are robust, the Scharr operator slightly edged out in performance for our applications. It consistently delivered more defined edges as can be seen in Figure 6.2, which proved advantageous for further image processing stages. Although both techniques are commendable, the Scharr method’s ability to maintain clear edge orientation makes it particularly beneficial for defining regions of interest in our studies. It is important to note, however, that the inherent variability in image contrast and contamination types limits the universal applicability of any edge detection method. Thus, our choice of Scharr primarily facilitates the initial identification of contamination areas, setting the stage for a subsequent detailed analysis. The resulting image serves for the further detection of Regions of Interest (ROI).

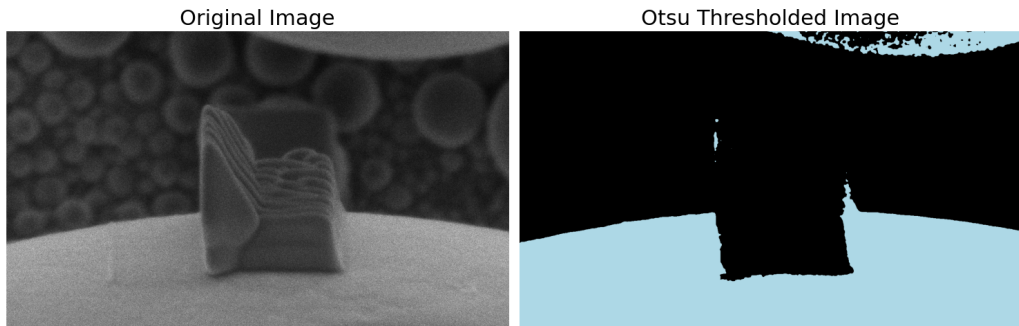


Figure 6.1: Comparison of the original and Otsu’s thresholded image.

Tin Ball edges

After preprocessing, the objective becomes to identify the extremities of the tin ball. Specifically, we aim to pinpoint the most left and right points where the tin ball ends and the background begins. This is important because, according to the analysis of the dataset,

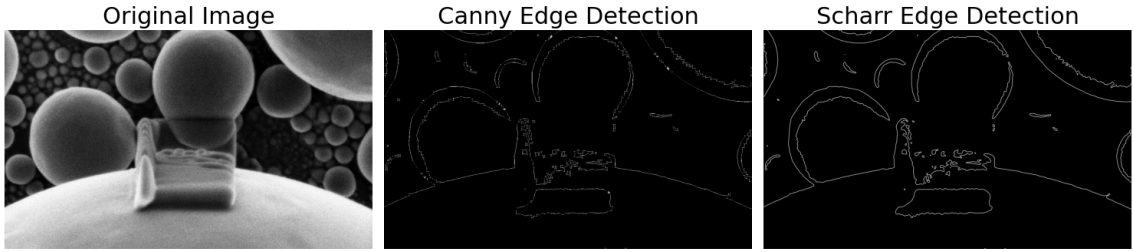


Figure 6.2: Comparative analysis of Canny and Scharr edge detection on a SEM image. This figure demonstrates the enhanced definition and clarity of boundaries achieved with the Scharr method, which proved particularly beneficial for identifying regions of interest within our dataset.

the bottom edge of contamination does not extend beyond these points. In other cases, the contamination is defined as low or none.

Extraction and Definition of the Region of Interest (ROI)

The goal is to accurately pinpoint and isolate the crucial Region of Interest (ROI) in the image. This is important because it allows for an in-depth inspection of the particular area affected by contamination.

- **Identification of Tin Ball Edges and Contour Validation:** The process starts with detecting the initial contour from the bottom center of the image. After this, the next step involves locating the contour's farthest left and right points. It is crucial to validate the contour width to ensure consistency across all contaminations. Additionally, the contour's height is checked against the tin ball's top edges to ensure that it does not exceed this limit, as exceeding could indicate zero contamination in the image, halting further analysis.
- **Detection of Contamination Layer Boundaries:** After validating the contour, the algorithm meticulously determines the left and right boundaries of the contamination layer. Then it is checked that the distance between these two points is not under 350 pixels. This threshold is established based on the scanning area, which is approximately 350 pixels in 1024x768 resolution images.
- **Extraction of ROI:** Once the boundaries have been defined, the Region of Interest (ROI) is extracted by trimming the original image from the contour's most left to its most right side. This refined segment represents the specific area of the image that encapsulates vital information about the contamination layer, thus ensuring that our analysis is focused and accurate.

By employing these steps, we lay a solid foundation for the subsequent analytical tasks, ensuring that the contamination is precisely localized.

Starting Point

The next phase focuses on pinpointing the initial point of analysis, strategically located midway between the contamination's upper and lower bounds. This determination relies

on analyzing vertical profile pixel values across each row within a central column that falls within our region of interest. To enhance measurement accuracy and mitigate potential distortions, we examine a breadth of 100 columns on either side of this central column. By averaging these values, we construct a vertical profile, as shown in Figure 6.3. Our approach involves extracting all local minima and maxima from this profile and sequentially evaluating these points from the highest to the lowest. Should the intensity shift between a given minimum and its nearest maximum exceed a threshold of 40, we consider this point as a candidate for our starting-point array. Empirically, we have found that a threshold of 40 is optimal for this purpose. In instances where no change exceeds the threshold, we systematically reduce it and reassess it, ensuring that at least one viable starting point is identified. Following the accumulation of potential starting points, we eliminate any that do not exceed the tin ball edge threshold, as discussed in the preceding section. Subsequently, we isolate the point that signifies the most significant variation between maximum values, which is marked for further analysis to delineate the upper and lower limits of contamination.

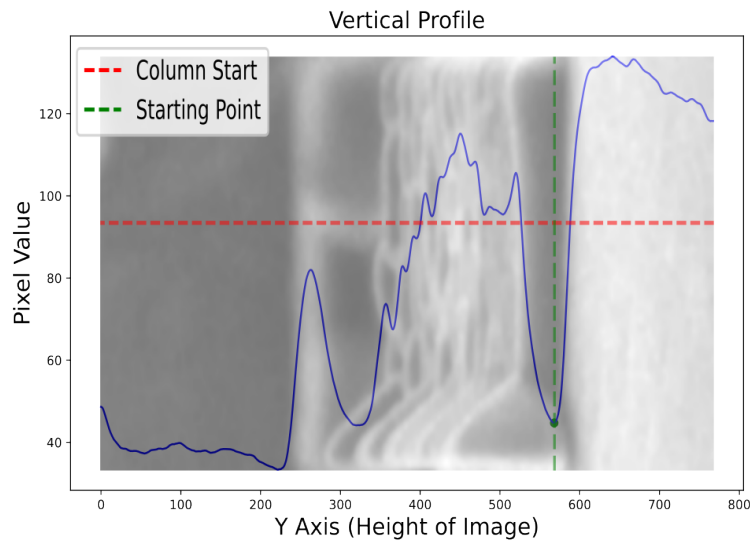


Figure 6.3: Vertical profile illustrating pixel values along the height of the image, with the identified starting point marked by green vertical dashed line. The ROI from the original image, rotated to align with the Y Axis, is displayed behind the plot.

Finding Bottom and Top of contamination

In this section, we enhance the methodology initiated to determine the starting point by employing a vertical plot analysis, similar to the initial steps taken. The gradient of this plot was computed using second-order accurate central differences for interior points and one-sided forward differences at the boundaries. This approach enables us to identify significant variations within our column of interest, thereby elucidating the regions that mark the top and bottom boundaries of the contamination.

Initially, we identify all local maxima and minima through a straightforward comparison of neighboring values in the gradient plot of our vertical line profile, and subsequently using the starting point established earlier as a benchmark, we examined the gradient plot to

isolate the most pronounced maximum that extends from the starting point towards the upper boundary of the image height. This maximum point effectively signifies the bottom edge of the contamination. The observable transition at this point, marked by a significant shift from the lighter hue of the tin ball to the darker shades that denote the contamination layer, provides visual confirmation of our computational findings, as illustrated in Figure 6.4

Subsequently, our attention turns towards identifying the contamination's upper boundary. Starting from the established point and moving towards the image's lower boundary, we search for the minimum that leads to a subsequent maximum with a biggest substantial variance in the direction towards the top of the image. The range where we set from bottom to top of the image is bottom of contamination plus 200 pixels defined according to the biggest height in our dataset is 178 so if we take in mind there might be chance of go over this value we set the range to find top from bottom plus 200 pixels towards the top of the image. This specific minimum, which also represents the upper limit of the contamination when approached from the bottom boundary, is thus identified as the top of the contamination.

Through the validation of gradient plots across our defined datasets, we have ascertained the effectiveness of this approach in pinpointing the vertical extents of contamination accurately, as will be mentioned in the next chapter, where we will discuss the error of this method 7.2. The approach highlights the effectiveness of gradient analysis not just as a method for boundary detection, but also as a useful tool for contamination measurement within the examined specimens.

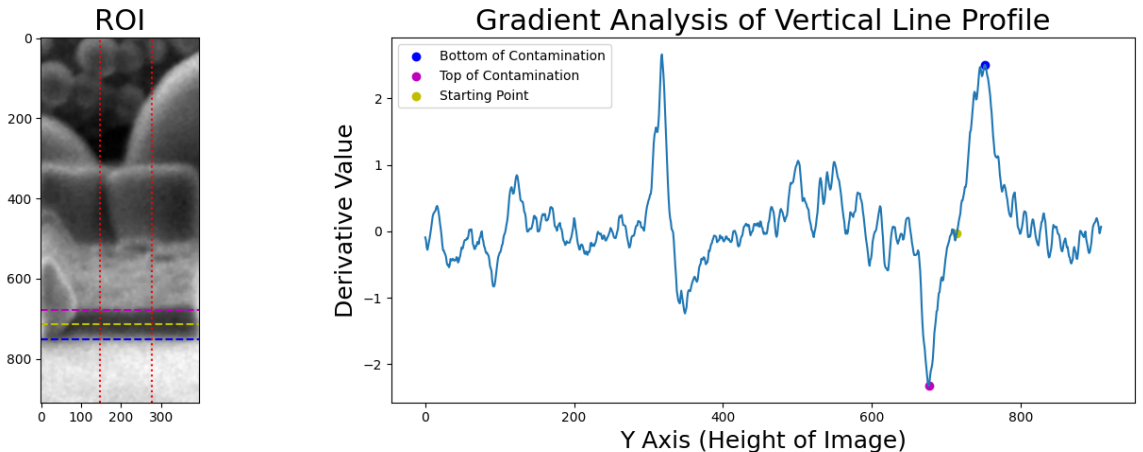


Figure 6.4: Illustration of the region of interest delineated by red lines indicating the source area for the vertical plot analysis. The contamination boundaries are highlighted with a purple line marking the top and a blue line denoting the bottom on the left side of the Figure. The right side features the corresponding gradient plot, showcasing the variation in intensity across these marked boundaries.

6.2 Method 2: DeepLabv3-based Contamination Layer Segmentation

This section details the technical implementation of the DeepLabv3 model customized for the segmentation of contamination layers in Scanning Electron Microscopy (SEM) images.

Covers the aspects of training the model using PyTorch [19], and post-processing techniques to refine the segmentation results.

Dataset Preparation

A critical aspect of implementation involves preparing the SEM image dataset to train the segmentation model. The dataset consists of SEM images, each manually annotated to delineate the contamination layers. The preparation of the dataset is discussed in a previous chapter 5.

Model Configuration

The DeepLabv3 model is configured and trained using PyTorch [19], a popular framework for deep learning applications due to its flexibility and extensive library support. The training process includes the following configurations and steps:

- **Model Architecture:** Our model employs the DeepLabv3 architecture [4], utilizing the ResNet-101 backbone for robust feature extraction. Initially pre-trained on a comprehensive dataset, the model is fine-tuned for a binary segmentation task that detects contamination at the pixel level. This fine-tuning involves adapting the output layer to produce a single-channel output, which classifies each pixel as either 'contaminated' or 'non-contaminated.' Such a modification is essential for aligning the model's capabilities with the binary classification demands of our dataset annotations.
- **Loss Function:** During the model's fine-tuning process, we utilize the Mean Squared Error (MSE) loss function. This loss function was selected due to its successful application in fine-tuning DeepLabv3 on cracks, as highlighted in the work by Minhas [15].
- **Optimizer and Learning Rate:** An Adam optimizer [12] with an initial learning rate of 0.0001 is used. The learning rate is adjusted according to a learning rate scheduler based on the validation loss to ensure effective learning without plateauing.

Model Performance Evaluation

In the book *Data Science for Business: What You Need to Know about Data Mining and Data-Analytic Thinking* by Foster Provost and Tom Fawcett [21], the authors underscore the role of evaluating a model's ability to accurately manage and predict data. The book elaborates on various key performance metrics for assessing the efficacy of classification models in the stages of the machine learning process. These metrics, including the Train and Test AUROC and F1 scores, are presented as indicators of the predictive precision of a model and its generalizability. This section provides an overview of what these metrics mean and their typical range, with more comprehensive details available in the book itself.

The F1 score, which ranges from 0 to 1, evaluates the balance between precision (the proportion of true positive results in all positive predictions) and recall (the proportion of true positive results in all actual positives). A higher F1 score suggests better balance and performance of the model. The AUROC (Area Under the Receiver Operating Characteristics), which also varies from 0 to 1, assesses the model's capability to differentiate between classes. Higher AUROC values suggest an enhanced ability to discriminate. Detailed discussions of these interpretations and additional explanations are provided in the previously mentioned book.

Detailed Training Loop

Training loop is component where the model is trained iteratively and evaluated against the datasets to optimize its performance. The detailed training loop is implemented in Python using PyTorch [19], and it operates as follows:

- **Setup Phase:** The model is initialized and transferred to a GPU if available to leverage hardware acceleration for training. This is critical for handling the computational demands of training DeepLabv3 on a dataset. A log file is created to record training and testing metrics for each epoch, which helps in monitoring the model's performance and diagnosing issues during training.
- **Epoch Execution:** The loop iterates through a specified number of epochs, where each epoch consists of both training and testing phases to validate the model's performance continually. For each epoch, the model state is toggled between the training and evaluation modes, using `model.train()` and `model.eval()`.
- **Batch Processing:** Within each epoch, data are processed in batches. For each batch, the images and their corresponding masks are loaded and transferred to the GPU. At the beginning of each batch, the gradient calculations are reset to prevent accumulation from previous iterations. This is done using `optimizer.zero_grad()`.
- **Forward and Backward Passes:** The model performs a forward pass to generate predictions for the batch. The loss is then calculated using a specified criterion, comparing the predicted output against the ground-truth mask labels. During the training phase, a backward pass is executed to compute gradients, and an optimization step is performed to update the model's weights.
- **Metrics Calculation and Logging:** For each batch we calculate F1 score and Auroc (area under the receiver operating characteristic curve) score. These metrics are then averaged over the epoch and logged in the previously created log file. The model's performance is assessed at the end of each epoch by comparing the current loss with the best loss observed in previous epochs. If an improvement is found, the model weights are updated to reflect the best performing model.
- **Completion and Model Saving:** Upon completion of all epochs, the training loop reports the total time taken and the best loss achieved. The best model weights are saved, ensuring that the most effective version of the model is preserved for future inference tasks.

This detailed implementation ensures rigorous training and validation, allowing the model to effectively learn from the training data while maintaining the ability to generalize to new, unseen images. The logging of detailed metrics provides an essential tool for tracking the model's progress and making informed adjustments to training parameters.

Post-processing

Once trained, the model is used to segment new SEM images. This involves the following post-processing steps to quantify contamination:

- **Model Inference:** For the application, the input images are first resized to fit the model’s expected input dimensions of 480×320 pixels. Each image is then restructured into a tensor format appropriate for the model, normalized, and processed through the network to obtain a prediction. The model outputs a probability map, from which we extract a binary mask by applying a threshold.
- **Thresholding:** In the thresholding section, we have developed a tool „Automation Mask Threshold Finder“ discussed in section 5.5. This tool, when provided with a dataset and a corresponding csv file containing values for the top, bottom, and height of each image, can determine the optimal threshold value. The goal is to minimize the mean error of the output from the fine-tuned model to the greatest extent possible and accurately delineate the foremost layer of contamination in the image for subsequent quantification.

Chapter 7

Experiments and Evaluation

This chapter details the experiments conducted with various datasets to evaluate the impact of fine-tuning on the model’s performance. The objective was to determine how different types of data affect the accuracy and robustness of the segmentation of the model. We evaluated the performance of the Edge Detection-Based Contamination Analyzer (EDCA) and the chosen fine-tuned DeepLabv3 model, focusing on their accuracy, precision, and error metrics compared to manually annotated ground truth data.

7.1 Model Experiments Across Datasets

- **Dataset with Contamination Only:** The initial experiment utilized a dataset comprising 339 images, all containing contamination. This dataset helped establish a baseline for the model’s ability to identify and segment contaminated areas without the influence of uncontaminated regions.
- **Mixed Contamination Dataset:** The second experiment incorporated a dataset that included both contaminated and uncontaminated images. This approach was intended to test the model’s discriminative power in distinguishing between contaminated and clean areas. The dataset consists of 563 images.
- **Augmented Dataset:** The final set of experiments employed an augmented dataset, where original images were modified using techniques detailed in section 5.4. The purpose was to evaluate the model’s robustness and its ability to maintain accuracy despite variations in image presentation and quality. This dataset is composed of 10 augmented versions for each image from the Contamination Only dataset, generated through the methods described in section 5.4, totaling 3390 images.

As highlighted in the work of Minhas et al. (2020) [15], our models demonstrate robust performance after fine-tuning for a relatively small number of epochs, fewer than 25. This is evident from the results shown in Figure 7.1, which presents the training outcomes exclusively on the Contamination Only dataset. Specifically, training and test losses show substantial reductions early in the training process, with training loss decreasing from 0.0214 to 0.0021 and test loss from 0.0142 to 0.0042 by the 25th epoch. Concurrently, the F1 scores and AUROC values also show remarkable improvement within this period, achieving levels above 0.88 and 0.94. This underscores the model’s capability for quick adaptation without a significant risk of overfitting, highlighting its efficiency in learning from limited data.

Upon fine-tuning the model using an augmented dataset, both the training and test losses exhibited a rapid decline, with the training loss reducing from 0.0046 to 0.0010 and the test loss from 0.0081 to 0.0015 over the initial 50 epochs. Concurrently, the F1 scores on both the training and test sets showed gradual improvement, starting at 0.469 and 0.384, and peaking at around 0.629 and 0.628 by the 30th epoch. This indicates a steady enhancement in the precision and recall of the model.

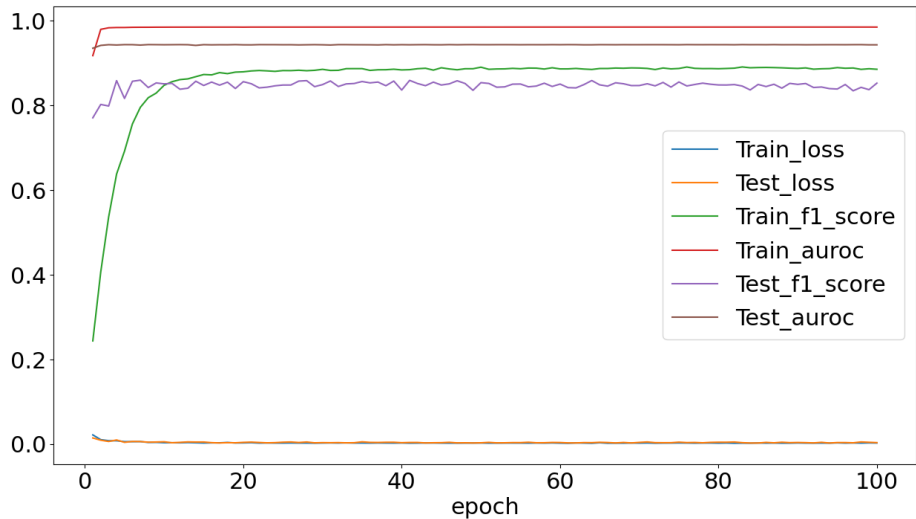


Figure 7.1: Training dynamics over epochs for a fine-tuned model on the Contamination Only dataset. The graph illustrates the evolution of loss and performance metrics, including the F1 score and area under the receiver operating characteristic curve (AUROC), for both training and test sets. Notably, the training loss rapidly declines within the first few epochs, stabilizing shortly thereafter. The F1 score and AUROC for the training set ascend correspondingly, indicating effective learning. Conversely, the test metrics plateau early, suggesting quick model generalization with minimal overfitting. These trends underscore the efficacy of fine-tuning with a modest epoch count.

Determination of Optimal Threshold Values

The efficacy of the finetuned models is contingent upon the calibration of threshold values. These values are determined through the use of the automated threshold finder, as elaborated in the preceding chapter that discusses dataset acquisition and annotation. Illustrative figures 7.2 therein depict the threshold variation for each iteration, outlining the impact on model performance. To determine the appropriate threshold, a dataset comprising all images merged into a single file was utilized. This approach ensures the selection of the most accurate threshold value, disregarding the data on which the model was previously trained. The optimal threshold value identified for the model refined exclusively on the Contamination-Only dataset is 0.41249, for the Mixed Contamination Dataset 0.44375, and for the Augmented dataset, the determined threshold is 0.42187. All corresponding data are saved in csv files, which are titled according to the dataset used for fine-tuning.

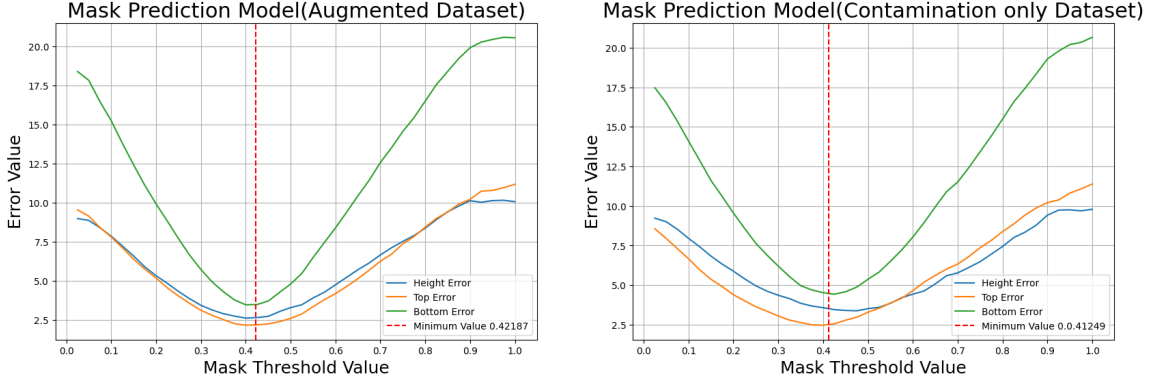


Figure 7.2: The figure illustrates a side-by-side comparison of error metrics for mask prediction models across a range of threshold values from 0.0 to 1.0. The left graph depicts the 'Mask Prediction Model (Augmented Dataset)' and identifies the optimal threshold where the combined error is minimized at approximately 0.42187, denoted by a dashed red line. The right graph represents the 'Mask Prediction Model (Contamination only Dataset)' with its minimal combined error threshold indicated at roughly 0.41249, also marked by a dashed red line. Both graphs plot three distinct error types: 'Height Error'(blue), 'Top Error'(orange), and 'Bottom Error'(green).

Comparison Between Contaminated and Mixed Dataset Models

This subsection evaluates the performance of models fine-tuned on different types of data sets: one trained exclusively on images with contamination and another trained on a mixed set of images, both contaminated and uncontaminated. The analysis was performed using a unique dataset that was not employed in the fine-tuning process to ensure an unbiased evaluation of the models' true performance.

The analysis focused on the output probability maps generated by each model. It was observed that the model fine-tuned on the mixed dataset tends to under-detect contamination, especially in images with very low levels of contamination. This results in a higher rate of false negatives, where the model fails to identify subtle contamination that might be perceptible upon close expert examination. This contrasts with the model trained only on contaminated datasets, which exhibited a tendency to identify contamination more reliably under the same conditions, albeit with a risk of overdetecting in some scenarios.

However, in situations with medium to high levels of contamination, both models showed similar effectiveness, accurately recognizing and delineating areas of contamination, as evidenced by their output probability maps.

To visually demonstrate these findings, Figure 7.3 contrasts the detection outputs of the two models, particularly highlighting their performance in scenarios where contamination is minimal and thus more challenging to detect.

Evaluation Metrics and Model Comparison

The efficacy of the segmentation models was quantitatively assessed through the Intersection over Union (IoU) metric in the following Equation 7.1, widely used to evaluate the accuracy of object detection and segmentation tasks. This metric measures the extent of overlap between the model-generated predicted segmentation masks and the manually annotated ground truth masks. For a more detailed explanation, refer to the book by Provost [21].

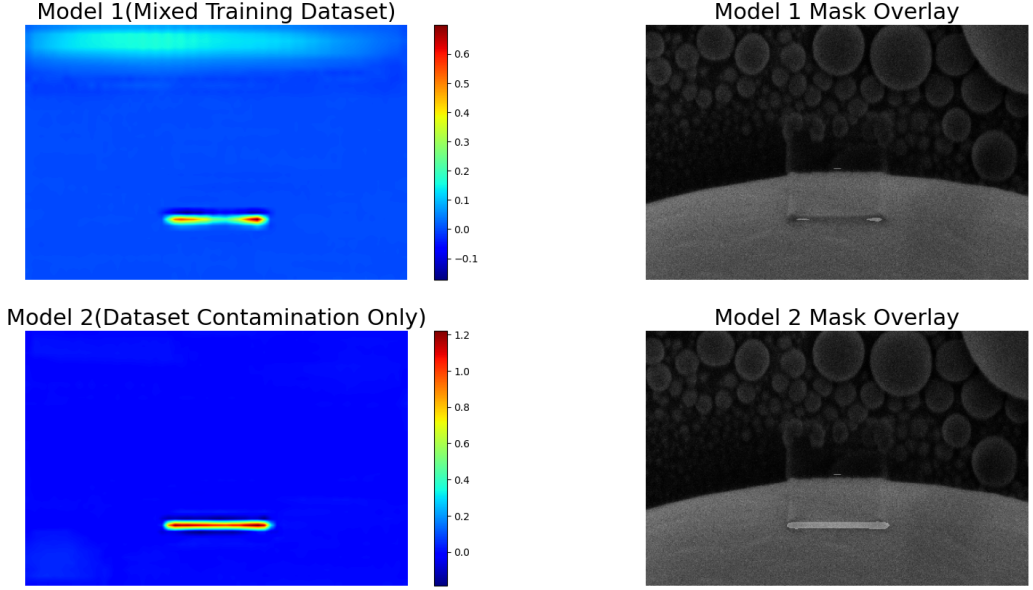


Figure 7.3: Comparison of probability maps and mask overlays: the top row shows the model trained on a mixed dataset failing to detect low levels of contamination, whereas the bottom row illustrates the model trained only on contamination datasets detecting such contamination more effectively.

$$d_{\text{IoU}}(X, Y) = 1 - \frac{|X \cap Y|}{|X \cup Y|} \quad (7.1)$$

In equation (7.1), $|X \cap Y|$ denotes the intersection of the predicted segmentation mask X and the ground truth mask Y , representing areas correctly identified by the model. $|X \cup Y|$ denotes the union of these masks, encompassing all areas identified by either or both. A higher IoU value indicates a greater overlap and hence a more accurate model.

A comparison was made between two distinct configurations of the DeepLabv3 model, each fine-tuned on different datasets: one on augmented images and the other on contamination only. This analysis employed a dataset composed of 54 unique SEM images, exclusively featuring contamination.

The performance of the models was assessed as follows:

- Model 1 achieved a mean IoU of 0.824 with a standard deviation of 0.078,
- Model 2 achieved a mean IoU of 0.832 with a standard deviation of 0.071.

Figure 7.4 illustrates the histogram of IoU scores for both models, demonstrating the distribution of scores and showcasing the slightly tighter spread and higher averages for Model 2.

The marginally better mean IoU score of Model 2 implies that it was more effective in precisely identifying contamination layers in SEM images. Additionally, the reduced standard deviation of Model 2 reflects its greater reliability across various testing conditions, making it the preferable option for use in precision-dependent environments. The enhanced accuracy and consistency of Model 2 offer a benefit for tasks that demand accurate contamination segmentation. The stability of Model 2 demonstrates its capability to manage

diverse imaging scenarios in the limits of our controlled environment and contamination levels, making it especially valuable in industrial settings where variations in SEM image conditions are common.

Conclusion

Model 2, with its higher mean IoU and lower variability, emerges as the preferred model for critical applications. Future work could explore further enhancements to the model's architecture or training process, such as integrating additional layers or advanced data-augmentation techniques, to further improve its accuracy and robustness, though the current level of accuracy is deemed sufficient for our purposes.

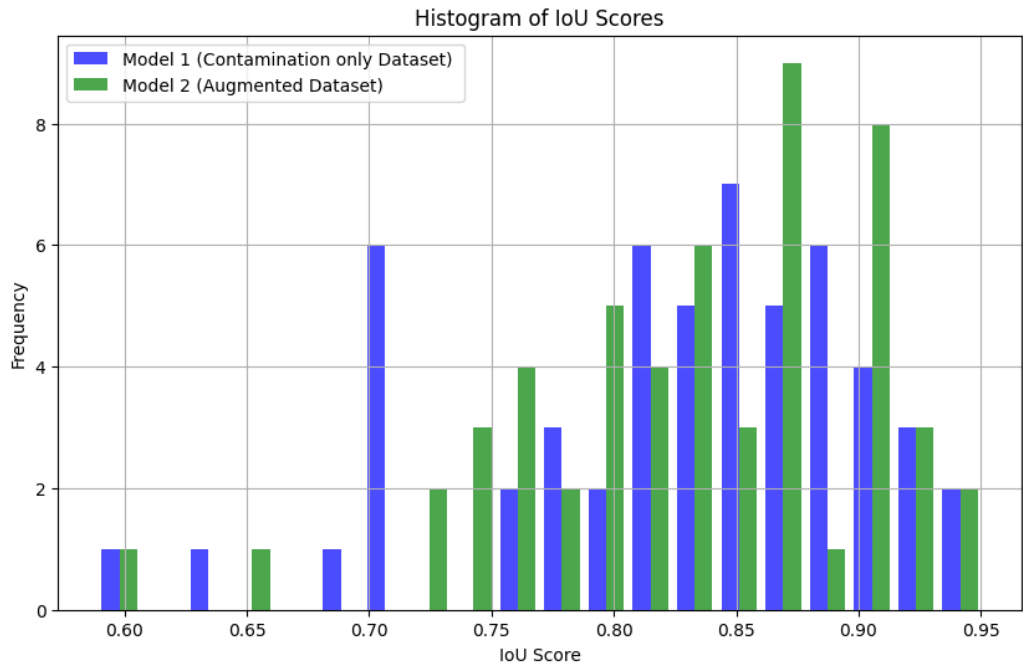


Figure 7.4: Histogram comparing IoU scores of Model 1 finetuned on Contamination only dataset(blue) and Model 2 finetuned on Augmented dataset(green), indicating that Model 2 not only has a higher average IoU but also shows less variability in performance across samples.

7.2 Error Analysis

This section delineates the error measurement methodologies employed for both the image processing technique and the machine learning model, comparing their accuracy against manually annotated ground truth data.

Error Measurement Procedure

Error measurements are conducted by comparing the predicted contamination dimensions of both detection methods against actual measurements derived from a manually annotated dataset.

- **Data Handling:** The SEM images along with their corresponding contamination measurements are stored in a CSV file. Each entry records the true dimensions of contamination for comparison.
- **Comparison Logic:** For each image, the absolute differences between the predicted and actual values of the key metrics are calculated: height, top and bottom of contamination.
- **Handling Special Cases:** Special attention is dedicated to images exhibiting minimal contamination, as detecting and quantifying low levels of contamination presents unique challenges. The primary objective is to accurately identify and define contamination within these images. In instances where contamination is minimal or is perceived incorrectly, when there is none, such results are excluded from our error measurement analysis. This exclusion is strategic, prioritizing the detection of any contamination over none to avoid skewing the overall analysis with potentially misleading data.

Statistical Error Metrics

Error quantification is achieved using several statistical metrics that provide information on the precision and consistency of the predictions made by each method (measurements are in pixels):

- **Mean Absolute Error (MAE):** Measures the average magnitude of the errors in a set of predictions, without considering their direction. The calculation of MAE is shown in Equation 7.2, where y_i are the true values, \hat{y}_i are the predicted values, and n is the number of observations.

$$\text{MAE} = \frac{1}{n} \sum_{i=1}^n |y_i - \hat{y}_i| \quad (7.2)$$

- **Mean Squared Error (MSE):** Highlights larger errors, which is particularly useful when large errors are particularly undesirable. The MSE is calculated using Equation 7.3, where y_i are the true values and \hat{y}_i are the predicted values. n represents the number of observations.

$$\text{MSE} = \frac{1}{n} \sum_{i=1}^n (y_i - \hat{y}_i)^2 \quad (7.3)$$

- **Root Mean Squared Error (RMSE):** Indicates the square root of the MSE, providing error measurement in the same units as the initial data, which simplifies interpretation. RMSE is detailed in Equation 7.4, where y_i are the true values, \hat{y}_i are the predicted values, and n is the number of observations.

$$\text{RMSE} = \sqrt{\frac{1}{n} \sum_{i=1}^n (y_i - \hat{y}_i)^2} \quad (7.4)$$

- **Median of Errors:** Indicates the median value of all absolute errors, providing a robust measure of central tendency that is less sensitive to outliers. The Median of

Errors is calculated as shown in Equation 7.5. It considers all absolute differences between predicted values \hat{y}_i and true values y_i .

$$\text{Median of Errors} = \text{median}(|y_1 - \hat{y}_1|, |y_2 - \hat{y}_2|, \dots, |y_n - \hat{y}_n|) \quad (7.5)$$

- **Success rate:** In our experiments, we establish a threshold such that the absolute difference between the values measured by our method and the ground truth does not exceed 20 pixels. The success rate is then calculated as the ratio of images meeting this criterion to the total number of images assessed, expressed as a percentage. This measurement is quantified in Equation 7.6.

$$\text{Success Rate (\%)} = \left(\frac{\text{Number of Images with Absolute Error} \leq 20 \text{ pixels}}{\text{Total Number of Images}} \right) \times 100 \quad (7.6)$$

Error Metrics for Edge Detection-Based Contamination Analyzer (EDCA) and DeepLabv3-based Contamination Layer Segmentation

The first method, an image processing technique to detect contamination and the machine learning model fine-tuned on augmented dataset showed the following error metrics which are shown in tables 7.1, 7.4, 7.2, 7.3:

Table 7.1: EDCA Error Metrics and Success Rates for the Contamination Only Dataset

| Method | Type | MAE | MSE | RMSE | Median | Success rate (%) |
|--------|--------|------|-------|------|--------|------------------|
| EDCA | Height | 6.15 | 53.68 | 7.33 | 6.00 | 81.17 |
| | Top | 3.32 | 17.93 | 4.23 | 3.00 | — |
| | Bottom | 5.15 | 42.18 | 6.49 | 4.00 | — |

Table 7.2: EDCA Error Metrics and Success Rates for the Default Dataset

| Method | Type | MAE | MSE | RMSE | Median | Success rate (%) |
|--------|--------|------|-------|------|--------|------------------|
| EDCA | Height | 6.15 | 53.72 | 7.33 | 6.00 | 87.16 |
| | Top | 3.32 | 17.89 | 4.23 | 3.00 | — |
| | Bottom | 5.18 | 42.52 | 6.52 | 4.00 | — |

Table 7.3: Comparison of EDCA and Model Error Metrics and Success Rates for the Unique Contamination Only Dataset

| Method | Type | MAE | MSE | RMSE | Median | Success rate (%) |
|--------|--------|-------------|--------------|-------------|-------------|------------------|
| EDCA | Height | 6.06 | 57.88 | 7.61 | 5.00 | 75.00 |
| | Top | 2.67 | 11.15 | 3.34 | 2.00 | — |
| | Bottom | 5.33 | 46.97 | 6.85 | 5.00 | — |
| Model | Height | 5.51 | 49.62 | 7.04 | 5.00 | 98.14 |
| | Top | 3.55 | 21.92 | 4.68 | 3.00 | — |
| | Bottom | 3.66 | 29.62 | 5.44 | 3.00 | — |

Table 7.4: Comparison of EDCA and Model Error Metrics and Success Rates for the Unique Dataset

| Method | Type | MAE | MSE | RMSE | Median | Success rate (%) |
|--------|--------|-------------|--------------|-------------|-------------|------------------|
| EDCA | Height | 6.06 | 57.88 | 7.61 | 5.00 | 87.18 |
| | Top | 2.67 | 11.15 | 3.34 | 2.00 | — |
| | Bottom | 5.33 | 46.97 | 6.85 | 5.00 | — |
| Model | Height | 5.56 | 50.40 | 7.10 | 5.00 | 98.61 |
| | Top | 3.54 | 22.04 | 4.69 | 3.00 | — |
| | Bottom | 3.71 | 30.17 | 5.49 | 3.00 | — |

Table 7.5: Comparison of EDCA and Model Error Metrics in nanometres for the Unique Contamination Only Dataset

| Method | Type | MAE | MSE | RMSE | Median |
|--------|--------|-------------|--------------|-------------|-------------|
| EDCA | Height | 7.90 | 103.47 | 10.17 | 6.74 |
| | Top | 3.27 | 18.46 | 4.30 | 2.25 |
| | Bottom | 7.02 | 85.09 | 9.22 | 5.62 |
| Model | Height | 7.27 | 80.83 | 8.99 | 5.62 |
| | Top | 4.47 | 35.41 | 5.95 | 3.37 |
| | Bottom | 5.14 | 51.02 | 7.14 | 3.37 |

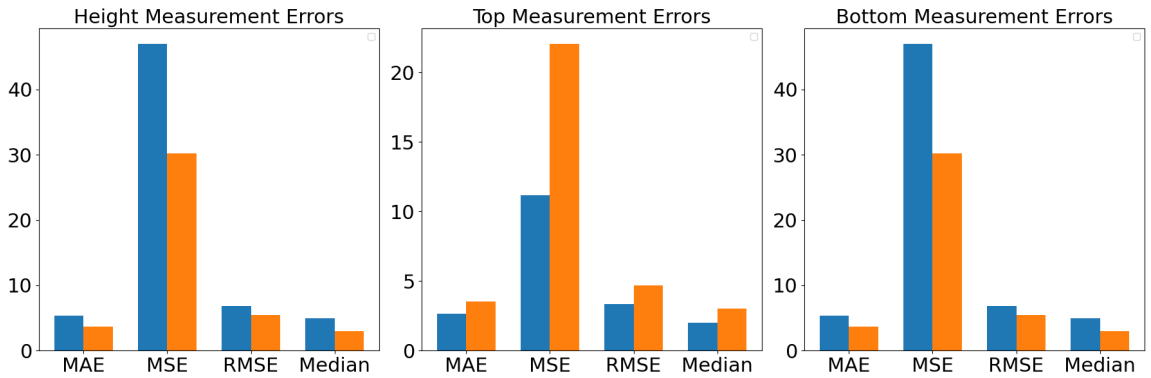


Figure 7.5: Visual comparison of error metrics for height, top, and bottom measurements for both the image processing technique and the machine learning model used on Unique Dataset. The blue columns signify EDCA, while the orange columns correspond to the Deeplabv3-based approach.

7.3 The precision of each method

Precision of each method in nanometers

Each image from a Scanning Electron Microscope (SEM) is associated with a specific pixel width that translates pixels into real-world units. This pixel width is given in meters; however, for the microscopic measurements, it's conventionally set to nanometers to enhance readability. In this experiment, to determine the measurement error of each method in nanometers, we collect the pixel width for each image, stored in a CSV file under the columns 'ImageName' and 'PixelWidth'. Subsequently, we can proceed with our predefined error measurement procedures, albeit with adjustments such as retaining the original image dimensions, since for performance reasons during testing, these were standardized to 1024x864. For each image, the bottom, top and height difference measurements from ground truth must be multiplied by the pixel width indicated in the CSV file. Ultimately, the calculation of the metrics remains consistent with the standard pixel-based error measurement method. The results of each method, displayed in nanometers, are detailed in Tables 7.5. Specifically, the precision of the height measurement in a unique dataset is 7.9 nanometers for the EDCA method and 7.27 nanometers for the model.

Edge Detection-Based Contamination Analyzer (EDCA)

The Edge Detection-Based Contamination Analyzer (EDCA) utilizes image processing techniques that excel in environments with clear, well-defined edges. However, its effectiveness diminishes under high-noise conditions or when processing images with subtle edge variations. Despite achieving low error values in controlled settings, as evidenced in Table 7.3, the EDCA method struggles with flexibility and adaptability to new or unseen variations that were not part of its initial training set.

The method's performance varies significantly based on the presence of contamination in images. For instance, it demonstrated an improved success rate, rising from 81.17% to 87.16%, when analyzing uncontaminated images. This improvement is documented across comparative analyses in Tables 7.1 and 7.2.

Figure 7.6 highlights specific cases where EDCA failed to detect both the bottom and height of contamination. In one depicted scenario, the contamination is excessively large, obscuring features like the leftmost peak, which is typically discernible in the dataset. This issue is compounded by a lack of distinct pixel value changes from the bottom to the top of the image, complicating the detection of the top of the contamination.

Moreover, the EDCA method struggles with variations in contamination build-up, which affect its detection capabilities. Another noted challenge is the method's sensitivity to changes in contrast, which can severely affect its ability to quantify contamination accurately. In conclusion the method is capable of measuring the contamination in most cases and even with good error values. The method performs often well despite variety in the contamination dataset, with the exception of the described edge cases.

DeepLabv3-based Contamination Layer Segmentation

The DeepLabv3-based model exhibited adaptability and robustness, showcasing its ability to generalize to new datasets effectively. This model achieved high accuracy in detecting contamination under various sample conditions, highlighting its precision in segmenting complex images. However, it is worth noting that the Edge Detection-Based Contamination

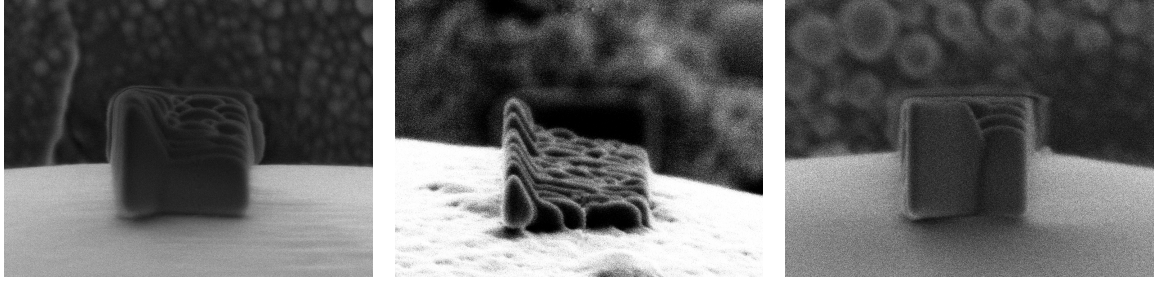


Figure 7.6: Illustration of EDCA’s performance limitations in specific cases: (a) Image lacking distinct edge variations leads to failure in top contamination detection, (b) Image with too complicated structure of contamination to detect, and (c) Image with too big contamination. These cases demonstrate the limited adaptability of the method to atypical scenarios not covered during its development phase.

Analyzer (EDCA) method exhibits slightly better performance in measuring the top of the contamination. This suggests a potential area for further optimization in DeepLabv3’s approach to detecting smaller, less distinct features. However, for accurate contamination assessment, it is crucial to measure the entire height of the contamination rather than just the top or bottom, in order to determine whether the contamination levels are excessively high or low.

Despite this challenge, the model’s robustness is evident across multiple evaluations. It accurately detects contamination in every analyzed image, with a particularly low mean error in height measurements, which are critical for our assessments. This performance is documented in the results of Tables 7.1, 7.2, 7.3, and 7.4.

The precision rate of the model in the unique dataset, as shown in Table 7.4, reaches 98.61% compared to manual measurements, underscoring its effectiveness with both trained and new data. This high level of accuracy supports the model’s utility in practical applications where reliable contamination detection is essential.

Discussion of Results

A comparative evaluation of both methods reveals that the model consistently outperforms EDCA in precision. The results from testing on the unique dataset demonstrated that the model achieved a precision of 98.61%, surpassing the precision of 87.18% recorded by the EDCA method. These metrics underscore the model’s adeptness in both identifying and quantifying contamination. In terms of error metrics for the detection of the bottom and the height of the contamination, the model’s performance excelled. Although EDCA registered slightly better performance in the detection of the top of the contamination, the overall analysis favors the DeepLabv3-based model for its effectiveness and reliability across various contamination scenarios. The measurement errors for each method, expressed in nanometers, are 7.13 nm for the model and 7.90 nm for EDCA.

Chapter 8

Conclusion and Future Work

In this study, we explored the effectiveness of various image processing techniques to measure the thickness of the contamination layers in scanning electron microscopy images. Two primary methods were proposed: a traditional image processing approach using Edge Detection-Based Contamination Analyzer (EDCA) and a modern machine learning approach through fine-tuning of the DeepLabv3 model on different datasets.

To facilitate accurate evaluation and comparison of these methods, we created datasets complete with annotations of ground truth masks and accompanying CSV files documenting the manually measured y-positions for each image. The ground truth masks were essential for training the machine learning model and validating both the finetuned model and the EDCA, providing a clear benchmark against which to measure the precision and robustness of each method.

Our evaluation highlights that while the Edge Detection-Based Contamination Analyzer (EDCA) provided a foundational approach for measuring contamination, it was the finetuned DeepLabv3 model that exhibited superior precision and robustness. The fine-tuned model, particularly when trained on an augmented dataset, demonstrated an improved ability to accurately segment and analyze contamination layers across diverse SEM images within the limits of our measurement setup. This was evidenced by significant improvements in evaluation metrics such as Intersection over Union (IoU) and reduced error rates in practical tests. Our model finetuned on Contamination only dataset achieved a mean IoU of 0.824 with a standard deviation of 0.078 and the model finetuned on the Augmented dataset achieved a mean IoU of 0.832 with a standard deviation of 0.071. These findings show a higher performance of the model fine-tuned on the Augmented dataset. Additionally, the mean error in nanometers was calculated for the height result of each method on a unique dataset, where the EDCA recorded 7.9 nm and the DeepLabv3 model recorded 7.27 nm, indicating the superior performance of the model. In comparison, the model achieved a success rate of 98.16% on the Unique dataset, while the EDCA achieved 87.16%, demonstrating the substantial robustness of the model.

Given these results, the decision was made to select the DeepLabv3 model fine-tuned on the augmented dataset. This choice was driven by the robustness of the model against various imaging challenges and its ability to deliver precise measurements to measure the height of contamination. Moreover, this research lays the groundwork for further studies focused on expanding the dataset and integrating additional machine learning models, potentially enhancing the precision of contamination evaluations, particularly for upper measurements where the model slightly underperformed compared to EDCA. It provides a pre-annotated dataset to other researchers, enabling them to evaluate different architectures or techniques.

Bibliography

- [1] AVERSA, R., CORONICA, P., DE NOBILI, C. and COZZINI, S. Deep Learning, Feature Learning, and Clustering Analysis for SEM Image Classification. *Data Intelligence*. One Rogers Street, Cambridge, MA 02142-1209, USA: MIT Press. october 2020, vol. 2, no. 4, p. 513–528. DOI: 10.1162/dint_a_00062. ISSN 2641-435X. Available at: https://doi.org/10.1162/dint_a_00062.
- [2] BIHANI, A., DAIGLE, H., SANTOS, J. E., LANDRY, C., PRODANOVIĆ, M. et al. MudrockNet: Semantic segmentation of mudrock SEM images through deep learning. *Computers & Geosciences*. 2022, vol. 158, p. 104952. DOI: <https://doi.org/10.1016/j.cageo.2021.104952>. ISSN 0098-3004. Available at: <https://www.sciencedirect.com/science/article/pii/S0098300421002387>.
- [3] BUSLAEV, A., IGLOVIKOV, V. I., KHVEDCHENYA, E., PARINOV, A., DRUZHININ, M. et al. Albumentations: Fast and Flexible Image Augmentations. *Information*. MDPI AG. february 2020, vol. 11, no. 2, p. 125. DOI: 10.3390/info11020125. ISSN 2078-2489. Available at: <http://dx.doi.org/10.3390/info11020125>.
- [4] CHEN, L., PAPANDREOU, G., SCHROFF, F. and ADAM, H. Rethinking Atrous Convolution for Semantic Image Segmentation. *ArXiv.org*. Ithaca: Cornell University Library, arXiv.org. june 2017, abs/1706.05587. ISSN 2331-8422. Available at: <http://arxiv.org/abs/1706.05587>.
- [5] EBRAHIMI, M. A., HOLST, M. and LUNASIN, E. The Navier-Stokes-Voight Model for Image Inpainting. *IMA Journal of Applied Mathematics*. january 2009, vol. 78. DOI: 10.1093/imamat/hxr069. Available at: <https://arxiv.org/abs/0901.4548>.
- [6] FILIPPO, M. P., DA FONSECA MARTINS GOMES, O., DA COSTA, G. A. O. P. and MOTA, G. L. A. Deep learning semantic segmentation of opaque and non-opaque minerals from epoxy resin in reflected light microscopy images. *Minerals Engineering*. 2021, vol. 170, p. 107007. DOI: <https://doi.org/10.1016/j.mineng.2021.107007>. ISSN 0892-6875. Available at: <https://www.sciencedirect.com/science/article/pii/S0892687521002363>.
- [7] GOLDSTEIN, J. I., NEWBURY, D. E., MICHAEL, J. R., RITCHIE, N. W. M., SCOTT, J. H. J. et al. *Scanning Electron Microscopy and X-Ray Microanalysis*. Fourthth ed. New York, NY: Springer Nature, 2018. ISBN 978-1-4939-6674-5.
- [8] GONZALEZ, R. C. *Digital image processing*. Fourth edition; Global editionth ed. New York: Pearson, 2018. ISBN 978-1-292-22304-9.

- [9] HUGENSCHMIDT, M., ADRION, K., MARX, A., MÜLLER, E. and GERTHSEN, D. Electron-Beam-Induced Carbon Contamination in STEM-in-SEM: Quantification and Mitigation. *Microscopy and Microanalysis*. december 2022, vol. 29, no. 1, p. 219–234. DOI: 10.1093/micmic/ozac003. ISSN 1431-9276. Available at: <https://doi.org/10.1093/micmic/ozac003>.
- [10] KAMANN, C. and ROTHER, C. Benchmarking the Robustness of Semantic Segmentation Models. *ArXiv.org*. Ithaca: Cornell University Library, arXiv.org. august 2019, abs/1908.05005. DOI: 10.1109/CVPR42600.2020.00885. Available at: <http://arxiv.org/abs/1908.05005>.
- [11] KIM, D., LEE, S., HONG, W., LEE, H., JEON, S. et al. Image Segmentation for FIB-SEM Serial Sectioning of a Si/C–Graphite Composite Anode Microstructure Based on Preprocessing and Global Thresholding. *Microscopy and Microanalysis*. october 2019, vol. 25, no. 5, p. 1139–1154. DOI: 10.1017/S1431927619014752. ISSN 1431-9276. Available at: <https://doi.org/10.1017/S1431927619014752>.
- [12] KINGMA, D. P. and BA, J. Adam: A Method for Stochastic Optimization. *ArXiv.org*. Ithaca: Cornell University Library, arXiv.org. 2017. ISSN 2331-8422. Available at: <https://arxiv.org/pdf/1412.6980.pdf>.
- [13] KUTÁLEK, J. *Measuring the thickness of material layers removed from a sample in an electron microscope*. Brno, 2023. Master’s Thesis. Brno University of Technology. Supervisor ING. MARTIN ČADÍK, P. doc.
- [14] LIU, J., LI, W., XIAO, C., HONG, B., XIE, Q. et al. Automatic Detection and Segmentation of Mitochondria from SEM Images using Deep Neural Network. In: *2018 40th Annual International Conference of the IEEE Engineering in Medicine and Biology Society (EMBC)*. IEEE, 2018, p. 628–631. DOI: 10.1109/EMBC.2018.8512393. ISBN 978-1-5386-3646-6. [Accessed: 2024-05-04]. Available at: <https://doi.org/10.1109/EMBC.2018.8512393>.
- [15] MINHAS, M. S. *Transfer Learning for Segmentation Using DeepLabv3 in PyTorch*. Dec 2019. Accessed: 2024-04-10. Available at: <https://towardsdatascience.com/transfer-learning-for-segmentation-using-deeplabv3-in-pytorch-f770863d6a42>.
- [16] MOROZ DUBENCO, C. Comparison of Gradient-Based Edge Detectors Applied on Mammograms. *Studia Universitatis Babes-Bolyai Informatica*. 2021, vol. 66, no. 2, p. 5–18. DOI: 10.24193/subbi.2021.2.01. ISSN 2065-9601. [cit. 2024-04-22]. Available at: <https://doi.org/10.24193/subbi.2021.2.01>.
- [17] OPENAI. *ChatGPT*. 2023. [cit. 2024-05-06]. Available at: <https://www.openai.com/chatgpt>.
- [18] OTSU, N. A Threshold Selection Method from Gray-Level Histograms. *IEEE Transactions on Systems, Man, and Cybernetics*. 1979, vol. 9, no. 1, p. 62–66. DOI: 10.1109/TSMC.1979.4310076. ISSN 0018-9472. [Accessed: 2024-05-04]. Available at: <https://doi.org/10.1109/TSMC.1979.4310076>.
- [19] PASZKE, A., GROSS, S., MASSA, F., LERER, A., BRADBURY, J. et al. PyTorch: An Imperative Style, High-Performance Deep Learning Library. *CoRR*. Ithaca: Cornell

University Library, arXiv.org. 2019, abs/1912.01703. ISSN 2331-8422. Available at: <http://arxiv.org/abs/1912.01703>.

- [20] POSTEK, M. T. An approach to the reduction of hydrocarbon contamination in the scanning electron microscope. *Scanning*. 1996, vol. 18, no. 4, p. 269–274. DOI: <https://doi.org/10.1002/sca.1996.4950180402>. Available at: <https://onlinelibrary.wiley.com/doi/abs/10.1002/sca.1996.4950180402>.
- [21] PROVOST, F. *Data science for business : what you need to know about data mining and data-analytic thinking*. 1st ed.th ed. Sebastopol: O'Reilly, 2013. Data Science/Business. ISBN 978-1-449-36132-7.
- [22] ROEDIGER, P., WANZENBOECK, H. D., HOCHLEITNER, G. and BERTAGNOLLI, E. Evaluation of chamber contamination in a scanning electron microscope. *Journal of Vacuum Science & Technology B: Microelectronics and Nanometer Structures Processing, Measurement, and Phenomena*. december 2009, vol. 27, no. 6, p. 2711–2717. DOI: 10.1116/1.3244628. ISSN 1071-1023. Available at: <https://doi.org/10.1116/1.3244628>.
- [23] SU, J., GE, J. and YANG, L. Study on thin film thickness measurement method based on digital image processing. In: ZHANG, Y., SASIAN, J. M., XIANG, L. and TO, S., ed. *5th International Symposium on Advanced Optical Manufacturing and Testing Technologies: Optical Test and Measurement Technology and Equipment*. Bellingham WA: SPIE, 2010, vol. 7656, no. 1, p. 765632–1–765636–6. DOI: 10.1117/12.864540. ISBN 081948086X. Available at: <https://doi.org/10.1117/12.864540>.
- [24] SUN, W., DUAN, F., ZHU, J., YANG, M. and WANG, Y. An Edge Detection Algorithm for SEM Images of Multilayer Thin Films. *Coatings*. 2024, vol. 14, no. 3. ISSN 2079-6412. Available at: <https://www.mdpi.com/2079-6412/14/3/313>.
- [25] VLADAR, A. and POSTEK, M. Electron Beam-Induced Sample Contamination in the SEM. *Microscopy and Microanalysis*. 2005, vol. 11, S02. DOI: 10.1017/S1431927605507785. ISSN 1431-9276. [Accessed: 2024-05-04]. Available at: <https://doi.org/10.1017/S1431927605507785>.
- [26] ZHOU, W., APKARIAN, R., WANG, Z. L. and JOY, D. Fundamentals of Scanning Electron Microscopy (SEM). In: ZHOU, W. and WANG, Z. L., ed. *Scanning Microscopy for Nanotechnology*. New York, NY: Springer New York, 2006, p. 1–40. DOI: 10.1007/978-0-387-39620-0_1. ISBN 978-0-387-33325-0. [Accessed: 2024-05-04]. Available at: https://doi.org/10.1007/978-0-387-39620-0_1.